CONTROLLED SENSITIVITY OF MARINE CONTROLLED-SOURCE ELECTROMAGNETIC SURVEYS

by

Daeung Yoon

A thesis submitted to the faculty of
The University of Utah
in partial fulfillment of the requirements for the degree of

Master of Science

in

Geophysics

Department of Geology and Geophysics

The University of Utah

May 2012

The University of Utah Graduate School

STATEMENT OF THESIS APPROVAL

The thesis of Daeung Yoon

has been approved by the following supervisory committee members:

Michael S. Zhdanov , Chair **08/08/11**
Date Approved

Erich U. Petersen , Member **08/13/11**
Date Approved

Alexander V. Gribenko , Member **08/05/11**
Date Approved

and by **D. Kip Solomon** , Chair of

the Department of **Geology and Geophysics**

and by Charles A. Wight, Dean of The Graduate School.

ABSTRACT

Based on the integrated sensitivity method, we introduce the concept of controlled sensitivity, which enables the sensitivity of a geophysical survey to be focused on a specific target area of sea bottom formation. In particular, we find the optimal parameters of the data weighing, which make it possible to increase the sensitivity of the survey within a specific area, where a potential geological target (e.g., a hydrocarbon reservoir) may be located. We demonstrate this approach with a numerical study of the sensitivity of the marine controlled-source electromagnetic (MCSEM) surveys, developing a numerical method and computer codes for constructing one-dimensional and two-dimensional controlled sensitivity for given a priori sensitivity models. This method represents an important technique to increase the resolution of MCSEM data with respect to a specific target area.

To my parents and Sungjin

CONTENTS

ACKNOWLEDGMENTS

I would like to acknowledge the financial and technical support of the Consortium for Electromagnetic Modeling and Inversion (CEMI) at the Department of Geology and Geophysics, University of Utah.

I would also like to express my deep gratitude to my advisor and committee chair, Dr. Michael Zhdanov, for giving me a chance to work under his guidance and with his great support on this research.

I would also like to thank my advisor, Dr. Erich U. Petersen, for helpful suggestions on this work, and sharing some of his diverse expertise.

I also thank my advisor, Dr. Alexander V. Gribenko, for helpful guidance on this work, and for answering numerous questions about programming and inversion techniques.

I would also like to thank Ms. Alexandra Kaputerko, for sharing the techniques to calculate the sensitivities, and providing invaluable program codes to refer for this research.

I would also like to thank Dr. Le Wan, and Dr. Masashi Endo, for priceless discussions related to this thesis research and addressing questions related to practical geophysical situations.

Finally, I would like to thank all my colleagues in the CEMI group. Without their support and encouragement, I could not have finished my research.

CHAPTER 1

INTRODUCTION

During recent years, marine controlled-source electromagnetic (MCSEM) surveys have become widely used for off-shore hydrocarbon exploration. The MCSEM method is based on the transmission of a low-frequency electromagnetic (EM) signal from a subsea source towed behind a ship and on the measurement of the EM response using a system of sea floor receivers. One of the most important questions in planning an MCSEM survey is whether the observed EM data are sensitive to prospective HC reservoirs. That is why many techniques for sensitivity analysis of EM data have been developed. The main idea of this thesis has been driven by another related question during the study of the sensitivity analysis, whether it is possible to control the sensitivity of the survey, focusing it on our desired specific target area of the sea bottom formations. In this thesis we introduce a method of solving this problem and demonstrate this method with numerical studies.

Traditionally, the sensitivity of a geophysical method is determined as the ratio of the variation of the data to the variation of the model parameters. Basically, there are three ways to calculate the sensitivities (McGillivray and Oldenburg, 1990). The most straightforward way to calculate the sensitivity is called “brute force” method or perturbation approach, which calculates the sensitivities using their finite-difference approximations. However, this method requires a large volume of computations and is extremely time-consuming because each sensitivity requires the solution of the forward problem with the corresponding parameter slightly perturbed (e.g., Edwards, Nobes and Gomez-Trevino, 1984). The second method is based on solving the sensitivity equation approach. In this method the initial operator is differentiated with respect to the model parameters and the subsequent boundary-value problem is solved (McGillivray et al., 1994). For the electromagnetic induction problem this approach has been used by Rodi (1976), Jupp and Vozoff (1976). The third method uses an adjoint operator. The sensitivities are computed using the solution to an adjoint Green's function problem (e.g., McGillivray and Oldenburg, 1990). It is well known that the approach based on adjoint operator is computationally the most efficient. However, when the surveys involve multiple transmitters and receivers, even the adjoint operator approach with the use of the reciprocity principle may not completely solve the sensitivity problem.

Kaputerko and Zhdanov (2010) introduced a more efficient technique for EM data sensitivity analysis in the case of MCSEM surveys executed with multiple transmitters and receivers. Their approach is based on the analysis of the integrated sensitivity of a survey. That allows the user to evaluate a cumulative response of the observed data to the conductivity perturbation for a survey with a multiple transmitter/receiver observation system. It is shown that, in a general case, the integrated sensitivity depends on many parameters, including survey design, frequencies, and conductivity distribution in the geoelectrical model. Kaputerko and Zhdanov (2010) also investigated the effect of data weighting on the integrated sensitivity. Based on the results of the numerical study, it was found that data weighting could dramatically affect the sensitivity distribution of the survey. This effect provides the methods to control the integrated sensitivity as well.

In this thesis we consider a possibility of using this effect in order to "focus" the sensitivity of the survey on a specific area of the sea bottom formation where a potential target - a hydrocarbon (HC) reservoir - may be located. This approach is based on the optimization of the integrated sensitivity of the MCSEM survey. We introduce a method of designing the data weights in such a way that the new weighted data would have a new integrated sensitivity with the desired (controlled) properties. I begin in Chapter 2 by describing the MCSEM method in offshore hydrocarbon exploration. Chapter 3 is a review of the integrated and the weighted integrated sensitivities that were introduced by Kaputerko and Zhdanov (2010). In Chapter 4, I describe the principles of the controlled sensitivity as well as the numerical solution to determine the optimal weights. That makes the integrated sensitivity focus on the specific target area. In Chapter 5 and 6, I demonstrate this concept by presenting the results of 1D and 2D controlled sensitivity, respectively, based on the basic MCSEM survey design. In both cases, our goal is to focus the sensitivity within the specific target interval (1D) and area (2D). I calculate the sensitivities with a synthetic survey based on the measurements of the E_x component of the electric field and the H_y component of the magnetic field, and analyze the results at various frequencies. I also present the maps of the optimal weights (called data weighting kernel matrix Q) determined by solving the controlled sensitivity problem. Finally, the major conclusions of this thesis are summarized in Chapter 7.

CHAPTER 2

MCSEM METHOD IN OFFSHORE HYDROCARBON EXPLORATION

In the end of the twentieth century, when the hydrocarbons exploration was moving from the continent to offshore, into progressively deeper water, seismic methods were still the dominant methods for the hydrocarbon exploration. However, alternative geophysical techniques are required to complement the seismic method because the seismic hydrocarbon indicators lack accuracy in marine geological terranes such as carbonate reefs, areas of volcanics and submarine permafrost (Edwards, 2005), and deepwater exploration wells are very expensive. Electromagnetics was not the first option among the alternative geophysical techniques because of a pervasive belief that the very conductive sea water precluded the application of electromagnetic systems for exploration. But this belief has been changed by a number of surveys which showed that various electromagnetic methods could be used quite effectively on and in the world's oceans (e.g.; Novysh and Fonarev, 1966; Trophimov and Fonarev, 1972; Dubrovskiy and Kondratieva, 1976). Now, the deepwater marine CSEM method has been widely used for hydrocarbon exploration since Charles Cox of Scripps Institution of Oceanography developed this method in the late 1970s (Cox, 1981) and carried out the first experiment on a mid-ocean ridge in the Pacific in 1979 (Spiess et al., 1980; Young and Cox, 1981).

This successful application of EM methods to offshore hydrocarbon exploration is based on the fact that EM enables us to distinguish between the very resistive target areas such as oil and gas reservoirs and the very conductive surrounding sea bottom formations filled with salt water. Therefore, the hydrocarbon reservoir is a very clear target for MCSEM.

The basic MCSEM survey is formed by a horizontal electric field transmitter, which is towed close to the sea floor to maximize the energy that couples to sea floor rocks, and a set of sea bottom electric and magnetic receivers. The currently widely used source in the industry is the long horizontal electric bipole (Constable and Srnka, 2007). The transmitter generates a powerful, low-frequency (typically from 0.1 to 10 Hz) EM signal propagating in all directions. The low frequencies penetrate deep into the conductive sea's bottom structures, while high frequencies contain little information about the subseafloor resistivity (MacGregor and Sinha, 2000). The signal returned from the sediments below the sea floor is recorded by a number of receivers, which are dropped from the survey vessel in the water and are sunk to the sea floor. Those receivers can measure all six components of the EM field, including E_z component which is close to zero on the earth surface on the land. The measured EM field is typically observed in time domain and is converted to the frequency domain using a Fourier transform.

After the completion of the field survey, EM inversion and imaging (migration) are performed to interpret the survey data, producing maps, cross sections, and 3D resistivity volumes that indicate the location of resistive bodies and the geoelectrical properties of the sea bottom formations (Zhdanov, 2010).

CHAPTER 3

INTEGRATED SENSITIVITY

I will review first the sensitivity analysis methods of MCSEM surveys that have been introduced by Kaputerko and Zhdanov (2010). In order to understand better the concept of the integrated sensitivity, we start with the basics of this concept, the integral equation method and the variation of EM fields in 3D model. We also describe a method for the Fréchet derivative calculation in order to solve numerically the integrated sensitivity problem. Finally, we introduce the weighted integrated sensitivity.

3.1 Integral equation method in three dimensions

Let us consider a 3D geoelectrical model with a background conductivity σ_b and local inhomogeneity D with an arbitrarily varying conductivity $\sigma = \sigma_b + \Delta\sigma$. We assume that $\mu = \mu_0 = 4\pi \times 10^{-7} \mathrm{H/m}$, where μ_0 is the free-space magnetic permeability. The model is excited by an electromagnetic field generated by an arbitrary source with an extraneous current distribution $\mathbf{j}^e$ concentrated within some local domain Q. This field is harmonic as $e^{-i\omega t}$. In this model, the electromagnetic field of an arbitrary current distribution $\mathbf{j}(\mathbf{r})$ can be determined by the electromagnetic Green's tensors $\widehat{\mathbf{G}}_E$, $\widehat{\mathbf{G}}_H$ (Zhdanov, 1988, 2002):

$$\mathbf{E}(\mathbf{r}_\mathrm{j}) = \iiint\limits_{D} \hat{\mathbf{G}}_\mathrm{E}(\mathbf{r}_\mathrm{j}|\mathbf{r}) \cdot \mathbf{j}(\mathbf{r})dv = \mathbf{G}_\mathrm{E}(\mathbf{j}),$$

$$\mathbf{H}(\mathbf{r}_\mathrm{j}) = \iiint\limits_{D} \hat{\mathbf{G}}_\mathrm{H}(\mathbf{r}_\mathrm{j}|\mathbf{r}) \cdot \mathbf{j}(\mathbf{r})dv = \mathbf{G}_\mathrm{H}(\mathbf{j}), \tag{3.1}$$

where $\mathbf{G}_\mathrm{E}$ and $\mathbf{G}_\mathrm{H}$ are the electric and magnetic Green's operators.

These equations (3.1) can be rewritten for the background medium with excess current $\mathbf{j}^\mathrm{a}$**:**

$$\mathbf{E}(\mathbf{r}_\mathrm{j}) = \mathbf{G}_\mathrm{E}(\mathbf{j}^\mathrm{a}) + \mathbf{G}_\mathrm{E}(\mathbf{j}^\mathrm{e}),$$

$$\mathbf{H}(\mathbf{r}_\mathrm{j}) = \mathbf{G}_\mathrm{H}(\mathbf{j}^\mathrm{a}) + \mathbf{G}_\mathrm{H}(\mathbf{j}^\mathrm{e}), \tag{3.2}$$

$$\mathbf{j}^\mathrm{a} = \Delta\sigma\mathbf{E} \tag{3.3}$$

where the first terms describe the anomalous fields generated by the excess currents

$$\mathbf{E}^\mathrm{a}(\mathbf{r}_\mathrm{j}) = \mathbf{G}_\mathrm{E}(\mathbf{j}^\mathrm{a}) = \mathbf{G}_\mathrm{E}(\Delta\sigma\mathbf{E}),$$

$$\mathbf{H}^\mathrm{a}(\mathbf{r}_\mathrm{j}) = \mathbf{G}_\mathrm{H}(\mathbf{j}^\mathrm{a}) = \mathbf{G}_\mathrm{H}(\Delta\sigma\mathbf{E}), \tag{3.3a}$$

and the second terms correspond to the background fields of the extraneous currents in the background media,

$$\mathbf{E}^\mathrm{b}(\mathbf{r}_\mathrm{j}) = \mathbf{G}_\mathrm{E}(\mathbf{j}^\mathrm{e}),$$

$$\mathbf{H}^\mathrm{b}(\mathbf{r}_\mathrm{j}) = \mathbf{G}_\mathrm{H}(\mathbf{j}^\mathrm{e}), \tag{3.4}$$

Summing both sides of expressions (3.2) and (3.3a), we finally obtain the well-known representation for the electromagnetic field as an integral over the excess currents in the inhomogeneous domain D (Raiche, 1974; Hohmann, 1975; Weidelt, 1975a):

$$\mathbf{E}(\mathbf{r}_j) = \mathbf{G}_E(\Delta\sigma\mathbf{E}) + \mathbf{E}^b(\mathbf{r}_j),$$
$$\mathbf{H}(\mathbf{r}_j) = \mathbf{G}_H(\Delta\sigma\mathbf{E}) + \mathbf{H}^b(\mathbf{r}_j), \tag{3.5}$$

Using these equations (3.5), we can calculate the electromagnetic field at any point $\mathbf{r}_j$, if the electric field is known within the inhomogeneity.

3.2 Calculation of the variation of the electromagnetic field for 3D models

In the 3D geoelectrical model, which we introduced in the previous section, the electromagnetic field satisfies the Maxwell's equations:

$$\nabla \times \mathbf{H} = \sigma\mathbf{E} + \mathbf{j}^e,$$
$$\nabla \times \mathbf{E} = i\omega\mu_0\mathbf{H}, \tag{3.6}$$

where $\mathbf{j}^e$ is the density of extraneous electric current.

Let us perturb the conductivity distribution $\sigma(\mathbf{r})$. Applying the perturbation operator to both sides of equations (3.6) we obtain the equations for corresponding variations of the electromagnetic field:

$$\nabla \times \delta\mathbf{H} = \sigma\delta\mathbf{E} + \delta\sigma\mathbf{E},$$
$$\nabla \times \delta\mathbf{E} = i\omega\mu_0\delta\mathbf{H}, \tag{3.7}$$

where $\delta\sigma$ is the conductivity variation, and $\delta\mathbf{H}, \delta\mathbf{E}$ are the corresponding variations of the magnetic and electric fields.

According to equations (3.1) the variations of the electric and magnetic fields, $\delta\mathbf{E}$ and $\delta\mathbf{H}$**,** can be found as the solutions of equations (3.5) as follows

$$\begin{aligned} \delta\mathbf{E}(\mathbf{r}_{\mathrm{j}}) &= \mathbf{G}_{\mathrm{E}}(\delta\sigma\mathbf{E}), \\ \delta\mathbf{H}(\mathbf{r}_{\mathrm{j}}) &= \mathbf{G}_{\mathrm{H}}(\delta\sigma\mathbf{E}). \end{aligned} \tag{3.8}$$

Using the definition of the Green's operators given by equations (3.8), we can express formulas in full form as follows:

$$\begin{aligned} \delta\mathbf{E}(\mathbf{r}') &= \iiint\limits_{\mathrm{D}} \widehat{\mathbf{G}}_{\mathrm{E}}(\mathbf{r}'|\mathbf{r}) \cdot \delta\sigma(\mathbf{r})\mathbf{E}(\mathbf{r})dv, \\ \delta\mathbf{H}(\mathbf{r}') &= \iiint\limits_{\mathrm{D}} \widehat{\mathbf{G}}_{\mathrm{H}}(\mathbf{r}'|\mathbf{r}) \cdot \delta\sigma(\mathbf{r})\mathbf{E}(\mathbf{r})dv. \end{aligned} \tag{3.9}$$

Substituting $\delta\sigma(\mathbf{r}) = \delta(\mathbf{r}'' - \mathbf{r})\delta\sigma_{\mathrm{v}}(\mathbf{r}'')$ in equations (3.9), we find the perturbations of the electric and magnetic fields, $\delta\mathbf{E}(\mathbf{r}')$, $\delta\mathbf{H}(\mathbf{r}')$, corresponding to the local perturbation of the integrated conductivity $\delta\sigma_{\mathrm{v}}(\mathbf{r}'')$ at a point $\mathbf{r}''$**:**

$$\delta\mathbf{E}(\mathbf{r}') = \widehat{\mathbf{G}}_{\mathrm{E}}(\mathbf{r}'|\mathbf{r}'')\delta\sigma_{\mathrm{v}}(\mathbf{r}'')\mathbf{E}(\mathbf{r}''), \tag{3.10}$$

$$\delta\mathbf{H}(\mathbf{r}') = \widehat{\mathbf{G}}_{\mathrm{H}}(\mathbf{r}'|\mathbf{r}'')\delta\sigma_{v}(\mathbf{r}'')\mathbf{E}(\mathbf{r}'')$$

3.3 Principle of integrated sensitivity

The integrated sensitivity $\mathrm{S_E}(\mathbf{r}'')$ of the data, collected over some surface Σ of observations over a frequency interval Ω, is equal to

$$\mathrm{S_E}(\mathbf{r}'') = \frac{\|\delta\mathbf{E}\|_{\Omega,\Sigma}}{\delta\sigma_{\mathrm{v}}} \tag{3.11}$$

where the $\mathrm{L_3}$ norm $\|\ldots\|_{\Omega,\Sigma}$ is determined by the formula

$$\|\delta\mathbf{E}\|_{\Omega,\Sigma} = \sqrt{\int_{\Omega}\iint_{\Sigma}|\delta\mathbf{E}(\mathbf{r}',\omega)|^2 ds' d\omega} \tag{3.12}$$

Substituting equations (3.10) into (3.12), we obtain the following expression for the integrated sensitivity of the electric field to the local perturbation of the conductivity at the point $\mathbf{r}''$:

$$\mathrm{S_E}(\mathbf{r}'') = \sqrt{\int_{\Omega}\iint_{\Sigma}\left|\widehat{\mathbf{G}}_{\mathrm{E}}(\mathbf{r}'|\mathbf{r}'')\cdot\mathbf{E}(\mathbf{r}'')\right|^2 ds' d\omega} \tag{3.13}$$

In a similar way we can find the integrated sensitivity of the magnetic field:

$$\mathrm{S_H}(\mathbf{r}'') = \sqrt{\int_{\Omega}\iint_{\Sigma}\left|\widehat{\mathbf{G}}_{\mathrm{H}}(\mathbf{r}'|\mathbf{r}'')\cdot\mathbf{E}(\mathbf{r}'')\right|^2 ds' d\omega} \tag{3.14}$$

3.4 The numerical method of computation of the integrated sensitivity

Formulas (3.12) and (3.13) can be used for practical computation of the integrated sensitivities if we know the corresponding Green's tensors, $\widehat{\mathbf{G}}_{\mathrm{E}}$ and $\widehat{\mathbf{G}}_{\mathrm{H}}$. However, the Green's tensor functions can be easily computed for relatively simple geoelectrical models only, e.g., for the horizontally layered media. In a general case, we should develop a corresponding numerical technique for solving this problem.

We can represent a numerical solution of the system of Maxwell’s equations in the form of a discrete operator equation:

$$\mathbf{d} = \mathbf{A}(\boldsymbol{\sigma}), \tag{3.15}$$

where $\mathbf{d} = (\mathrm{d}_1, \mathrm{d}_2, \mathrm{d}_3, \ldots \mathrm{d}_{\mathrm{N_d}})$ is a vector of the observed EM data, $\boldsymbol{\sigma} = (\sigma_1, \sigma_2, \sigma_3, \ldots \sigma_{\mathrm{N_m}})$ is a vector formed by the conductivity distribution in the model, and **A** is a forward modeling operator which is used for solving the system of Maxwell’s equations.

Applying the variational operator to both sides of equation (3.15), we obtain:

$$\delta\mathbf{d} = \mathbf{F}\delta\boldsymbol{\sigma}, \tag{3.16}$$

where F is the Fréchet derivative matrix of the forward modeling operator **A**.

Let us analyze the sensitivity of the EM data to the perturbation of one specific parameter, $\delta\sigma_{\mathrm{k}}$. To solve this problem, we write equation (3.15) in matrix notations:

$$\delta \mathrm{d}_{\mathrm{i}} = \mathrm{F}_{\mathrm{ik}}\delta\sigma_{\mathrm{k}}. \tag{3.17}$$

In the last formula, $\mathrm{F_{ik}}$ are the elements of the Fréchet derivative matrix **F** of the forward modeling operator, and there is no summation over index k. The norm of the perturbed vector of the data can be calculated as

$$\|\delta\mathbf{d}\| = \sqrt{\sum_{\mathrm{i}} \delta \mathrm{d_i} \delta \mathrm{d_i^*}} = \sqrt{\sum_{\mathrm{i}} (\mathrm{F_{ik}} \mathrm{F_{ik}^*}) \delta\sigma_{\mathrm{k}}}, \tag{3.18}$$

The integrated sensitivity of the data to parameter $\delta\sigma_{\mathrm{k}}$ is determined as the ratio (Zhdanov, 2002):

$$\mathrm{S_k} = \frac{\|\delta\mathbf{d}\|}{\delta\sigma_{\mathrm{k}}} = \sqrt{\sum_{\mathrm{i}} (\mathrm{F_{ik}} \mathrm{F_{ik}^*})}, \tag{3.19}$$

One can see that the integrated sensitivity of the data to the different parameters $\delta\sigma_{\mathrm{k}}$ varies because the contributions of the different parameters to the observation are also variable. A diagonal matrix with the diagonal elements equal to $\mathrm{S_k} = \frac{\|\delta\mathbf{d}\|}{\delta\sigma_{\mathrm{k}}}$ is called *an integrated sensitivity matrix*:

$$\mathbf{S} = \mathrm{diag}\left(\sqrt{\sum_{\mathrm{i}} (\mathrm{F_{ik}} \mathrm{F_{ik}^*})}\right) = \mathrm{diag}(\mathbf{F}^*\mathbf{F})^{1/2}. \tag{3.20}$$

Matrix **S** is formed by the norms of the columns of the Fréchet derivative matrix **F**.

3.5 Fréchet derivative calculation

In order to compute the integrated sensitivity, one has to determine the Fréchet derivative matrix F. An effective way of solving this problem is based on the Fréchet derivative calculation using a quasi-analytical approximation for a variable background (QAVB) developed by Gribenko and Zhdanov (2007). According to this method, we have the following integral representations for the Fréchet derivative of the electric and magnetic fields:

$$\left.\frac{\delta \mathbf{E}(\mathbf{r}_j)}{\delta \sigma(\mathbf{r})}\right|_{\Delta\sigma_a} = \mathbf{F}_E(\mathbf{r}_j|\mathbf{r}),$$
$$\left.\frac{\delta \mathbf{H}(\mathbf{r}_j)}{\delta \sigma(\mathbf{r})}\right|_{\Delta\sigma_a} = \mathbf{F}_H(\mathbf{r}_j|\mathbf{r}) \qquad (3.21)$$

The vector functions $\mathbf{F}_E$ and $\mathbf{F}_H$ are the kernels of the integral Fréchet derivative operators:

$$\mathbf{F}_{E,H}(\mathbf{r}_j|\mathbf{r}) = \left[\frac{1}{1-g^Q(\mathbf{r})}\widehat{\mathbf{G}}_{E,H}(\mathbf{r}_j|\mathbf{r}) + \widehat{\mathbf{K}}(\mathbf{r}_j|\mathbf{r})\right]\mathbf{E}(\mathbf{r}) \qquad (3.22)$$

and

$$\widehat{\mathbf{K}}(\mathbf{r}_j|\mathbf{r}) = \iiint_D \frac{\delta\sigma(\mathbf{r})}{\left(1-g^Q(\mathbf{r}')\right)^2}\widehat{\mathbf{G}}_E(\mathbf{r}_j|\mathbf{r}')\cdot\mathbf{E}(\mathbf{r}')\left[\frac{\mathbf{E}^*(\mathbf{r}')}{\mathbf{E}(\mathbf{r}')\cdot\mathbf{E}^*(\mathbf{r}')}\cdot\widehat{\mathbf{G}}_E(\mathbf{r}'|\mathbf{r})\right]dv', \qquad (3.23)$$

where $\widehat{\mathbf{G}}_E(\mathbf{r}_j|\mathbf{r})$ and $\widehat{\mathbf{G}}_H(\mathbf{r}_j|\mathbf{r})$ are the electric and magnetic Green's tensors defined for an unbounded conductive medium with the normal (horizontally layered) conductivity σ_n, and domain D represents a volume with the anomalous conductivity distribution $\sigma(\mathbf{r}) = \sigma_n + \Delta\sigma(\mathbf{r}), \mathbf{r} \in D$.

Function g^Q is determined by the following expression:

$$\mathrm{g}^{\mathrm{Q}}(\mathbf{r}) = \frac{\mathbf{E}^{\delta\sigma}(\mathbf{r}) \cdot \mathbf{E}^{*}(\mathbf{r})}{\mathbf{E}(\mathbf{r}) \cdot \mathbf{E}^{*}(\mathbf{r})}, \tag{3.24}$$

where $\mathbf{E}^{\delta\sigma}$ is the anomalous electric field:

$$\mathbf{E}^{\delta\sigma} = \iiint_{\mathrm{D}} \widehat{\mathbf{G}}_{\mathrm{E}}(\mathbf{r}_{\mathrm{j}}|\mathbf{r}) \cdot \delta\sigma(\mathbf{r})\mathbf{E}(\mathbf{r})dv. \tag{3.25}$$

It follows immediately from expressions (3.23) and (3.24) that, if $\delta\sigma \to 0$, then $\widehat{\mathbf{K}} \to 0$ and $\mathrm{g}^{\mathrm{Q}} \to 0$. In this case equation (3.22) can be simplified:

$$\mathbf{F}_{\mathrm{E,H}}(\mathbf{r}_{\mathrm{j}}|\mathbf{r}) = \widehat{\mathbf{G}}_{\mathrm{E,H}}(\mathbf{r}_{\mathrm{j}}|\mathbf{r})\mathbf{E}(\mathbf{r}) \tag{3.26}$$

The corresponding numerical method of the Fréchet derivative computations is based on the discrete form of the explicit integral expressions (3.22) or (3.26), which simplifies all calculations dramatically.

3.6 Weighted integrated sensitivity

In the case of the MCSEM survey, the observed data are usually normalized by the amplitude of the background field. In other words, we usually work with the weighted data:

$$\mathbf{d}_{\mathrm{w}} = \mathbf{W}_{\mathrm{d}}\mathbf{d}, \tag{3.27}$$

where $\mathbf{W}_{\mathrm{d}}$ is the data weighting matrix, as described below. The integrated sensitivity of the weighted data to the parameter $\delta\sigma_{\mathrm{k}}$ is determined according to the following formula:

$$\mathrm{S}_{\mathrm{wk}}=\frac{\|\delta\mathbf{d}_{\mathrm{w}}\|}{\delta\sigma_{k}}. \tag{3.28}$$

Formula (3.20) for the weighted integrated sensitivity matrix takes this form:

$$\mathbf{S}_{\mathrm{w}}=\operatorname{diag}(\mathbf{F}^{*}\mathbf{W}_{\mathrm{d}}^{*}\mathbf{W}_{\mathrm{d}}\mathbf{F})^{\frac{1}{2}}. \tag{3.29}$$

Taking into account that the weighted data are dimensionless, we immediately conclude that the weighted sensitivities S_{wk} are measured in the units of the resistivity, Ohm-m.

There are various methods for computing the data weights. Here we use the simplest approach based on the method of the error propagation for azimuth data (Morten, 2009). In order to determine a diagonal matrix of data weights $\mathbf{W}_{\mathrm{d}}$ of MCSEM data, we need to consider the source-receiver configuration. The first step is to estimate the orientation of the receivers and the source towline, and rotate the data to make the measurements at the receivers be oriented to the one axis, parallel to the source towline. The resulting in-line rotated field components are given by

$$\begin{pmatrix}B_x\\B_y\end{pmatrix}=\begin{pmatrix}\cos ø & \sin ø\\-\sin ø & \cos ø\end{pmatrix}\begin{pmatrix}B_a\\B_b\end{pmatrix}, \tag{3.30}$$

where B_l represents a horizontal component ($l=x,y$ for rotated data, or a,b for the data before rotation) of the electric (**B=E**) or magnetic (**B=H**) field, and ø is the estimated angle between the direction of the channel B_a of the sea floor receiver and the source towline direction.

On the second step, we calculate the magnitude of in-line rotated data:

$$|B_x|=\sqrt{|B_a|^2\cos^2 ø+|B_b|^2\sin^2 ø}, \tag{3.31}$$

$$\left|B_y\right| = \sqrt{|B_a|^2 \sin^2 ø + |B_b|^2 \cos^2 ø}. \tag{3.32}$$

To simplify equations (3.31) and (3.32), let us consider an ideal case where a channel E_a of a receiver is located parallel to the source towline, which will be used in our basic MCSEM surveys later. In this ideal case, the angle ø becomes zero and there only exist the data of the E_a and the H_b. Then, the magnitudes of in-line E_x and cross-line H_y data become

$$|E_x| = |E_a|, \tag{3.33}$$

$$\left|H_y\right| = |H_b|. \tag{3.34}$$

Lastly, we calculate a diagonal matrix of data weights $\mathbf{W}_\mathrm{d}$, whose component is an inverse absolute value of a magnitude of the corresponding background field.

$$\mathrm{W}_{d(i)}^{B_\kappa} = \frac{1}{\left|B_{\kappa(i)}^{b}\right|} \tag{3.35}$$

where the index κ denotes a horizontal component ($\kappa = x, y$) of the background electric ($\mathbf{B}^\mathrm{b} = \mathbf{E}^\mathrm{b}$) or background magnetic ($\mathbf{B}^\mathrm{b} = \mathbf{H}^\mathrm{b}$) field, which is the field generated by the transmitter in the horizontally layered background model of the earth, and the index (i) corresponds to the component, d_i, of a vector, $\mathbf{d} = (\mathrm{d}_1, \mathrm{d}_2, \mathrm{d}_3, \dots \mathrm{d}_{\mathrm{N_d}})$, of the observed EM data.

Applying equations (3.33) and (3.34) to (3.35), the data weighting matrix $\mathbf{W}_\mathrm{d}$ for the $\mathrm{E_x}$ component and the $\mathrm{H_y}$ component become

$$\mathbf{W}_d^{E_x} = \begin{bmatrix} \frac{1}{\left|E_{x1}^b\right|} & 0 & \cdots & 0 \\ 0 & \frac{1}{\left|E_{x2}^b\right|} & 0 & \vdots \\ \vdots & 0 & \ddots & 0 \\ 0 & \cdots & 0 & \frac{1}{\left|E_{xN_d}^b\right|} \end{bmatrix} \tag{3.36}$$

$$\mathbf{W}_d^{H_y} = \begin{bmatrix} \frac{1}{\left|H_{y1}^b\right|} & 0 & \cdots & 0 \\ 0 & \frac{1}{\left|H_{y2}^b\right|} & 0 & \vdots \\ \vdots & 0 & \ddots & 0 \\ 0 & \cdots & 0 & \frac{1}{\left|H_{yN_d}^b\right|} \end{bmatrix}. \tag{3.37}$$

CHAPTER 4

CONTROLLED INTEGRATED SENSITIVITY

4.1 Principles of controlled sensitivity

In practical applications we would like to design such weights, $\mathbf{W}_\mathrm{c}$, so that the corresponding integrated sensitivity, $\mathbf{S}_\mathrm{c}$, will be close or equal to the a priori preselected sensitivity $\mathbf{P}$:

$$\mathbf{S}_\mathrm{c} = \mathrm{diag}(\mathbf{F}^* \mathbf{W}_\mathrm{c}^* \mathbf{W}_\mathrm{c} \mathbf{F})^{\frac{1}{2}} \approx \mathbf{P}, \tag{4.1}$$

where $\mathbf{P}$ is a diagonal matrix with positive components. We will call the integrated sensitivity $\mathbf{S}_\mathrm{c}$, determined according to formula (4.1), a *controlled integrated sensitivity*.

The goal is to create a survey with controlled sensitivity to the target (a potential HC reservoir) located within a specific area of interest. It would be important if we could design data weights, which would increase the sensitivity of the survey to the target located within a specific depth interval. We will discuss the principles of solving this problem below.

First of all, we assume that the data weighting matrix $\mathbf{W}_\mathrm{c}$ is not necessarily diagonal. Let us find arbitrary data weighting matrix $\mathbf{W}_\mathrm{c}$, which would satisfy condition (4.1):

$$\mathrm{diag}(\mathbf{F}^*\mathbf{W}_\mathrm{c}^*\mathbf{W}_\mathrm{c}\mathbf{F}) \approx \mathbf{P}^2, \tag{4.2}$$

where we define the dimensions of all corresponding matrices as follows:

$$\mathbf{P} = [\mathrm{N_m} \times \mathrm{N_m}], \qquad \mathbf{F} = [\mathrm{N_d} \times \mathrm{N_m}], \qquad \mathbf{W}_\mathrm{c} = [\mathrm{N_d} \times \mathrm{N_d}]. \tag{4.3}$$

We introduce the following notations for $[\mathrm{N_d} \times \mathrm{N_d}]$ matrix $\mathbf{W}_\mathrm{c}^*\mathbf{W}_\mathrm{c}$:

$$\mathbf{Q} = \mathbf{W}_\mathrm{c}^*\mathbf{W}_\mathrm{c}, \qquad \mathbf{Q} = [\mathrm{N_d} \times \mathrm{N_d}]. \tag{4.4}$$

We will call matrix $\mathbf{Q}$ a data weighting kernel matrix. Note that the kernel matrix $\mathbf{Q}$ is a real symmetrical matrix.

In principle, one can find matrix $\mathbf{W}_\mathrm{c}$ from equation (4.4), if matrix $\mathbf{Q}$ is known. However, in fact, the corresponding inversion algorithms for the weighted data require knowledge of data weighting kernel matrix $\mathbf{Q}$ only (Zhdanov, 2002). Indeed, it can be demonstrated that an application of the data weights to the observed data is translated in the corresponding inversion algorithm in the calculation of the weighted data $\mathbf{d}_{\mathrm{W^*W}}$, only:

$$\mathbf{d}_{\mathrm{W^*W}} = \mathbf{W}_\mathrm{c}^*\mathbf{W}_\mathrm{c}\mathbf{d} = \mathbf{Q}\mathbf{d}. \tag{4.5}$$

Therefore, we will focus now on determining the matrix $\mathbf{Q}$ only from the corresponding equation arising from equation (4.2):

$$\mathrm{diag}(\mathbf{F}^*\mathbf{Q}\mathbf{F}) \approx \mathbf{P}^2. \tag{4.6}$$

Expression (4.6) describes a linear system, which has more equations than unknown components of matrix $\mathbf{Q}$, because usually we have more model parameters than the data ($\mathrm{N_d} \ll \mathrm{N_m}$). Thus we have an overdetermined problem. Therefore, we cannot find the data weighting matrix which would provide the exact solution to equation (4.6). In this situation, the following least squares equations can be substituted for matrix equation (4.6):

$$\begin{aligned}\Phi(\mathbf{Q}) &= \mathrm{diag}[(\mathbf{S}_{\mathrm{c}}^2 - \mathbf{P}^2)^*(\mathbf{S}_{\mathrm{c}}^2 - \mathbf{P}^2)] \\ &= \mathrm{diag}[(\mathbf{F}^*\mathbf{Q}\mathbf{F} - \mathbf{P}^2)^*(\mathbf{F}^*\mathbf{Q}\mathbf{F} - \mathbf{P}^2)] = \min,\end{aligned} \tag{4.7}$$

where $\Phi(\mathbf{Q})$ is a diagonal matrix,

$$\Phi(\mathbf{Q}) = \begin{bmatrix} \varphi_1 & 0 & \dots & 0 \\ 0 & \varphi_1 & 0 & \dots \\ \dots & 0 & \dots & \dots \\ 0 & \dots & \dots & \varphi_{\mathrm{N_m}} \end{bmatrix}, \tag{4.8}$$

formed by the misfits between the corresponding components of the preselected and controlled integrated sensitivities, respectively:

$$\varphi_{\mathrm{k}} = \left(\mathrm{S}_{\mathrm{ck}}^2 - \mathrm{P}_{\mathrm{k}}^2\right)^*\left(\mathrm{S}_{\mathrm{ck}}^2 - \mathrm{P}_{\mathrm{k}}^2\right) = \left|\mathrm{S}_{\mathrm{ck}}^2 - \mathrm{P}_{\mathrm{k}}^2\right|^2 \tag{4.9}$$

A global misfit functional $\varphi(\mathbf{Q})$ describing the accuracy of solving the entire system of linear equations (4.2) can be defined as a trace of matrix $\Phi(\mathbf{Q})$:

$$\begin{aligned}\varphi(\mathbf{Q}) &= \mathrm{Spur}[\Phi(\mathbf{Q})] \\ &= \mathrm{Spur}[(\mathbf{F}^*\mathbf{Q}\mathbf{F} - \mathbf{P}^2)^*(\mathbf{F}^*\mathbf{Q}\mathbf{F} - \mathbf{P}^2)] = \sum_{\mathrm{k}=1}^{\mathrm{N_m}} \varphi_{\mathrm{k}} = \min.\end{aligned} \tag{4.10}$$

A numerical algorithm for solving minimization problem (4.10) is provided in the next section. After matrix $\mathbf{Q}$ is determined, we can find the controlled sensitivity from a simple matrix formula:

$$\mathbf{S}_{\mathrm{c}} = \mathrm{diag}(\mathbf{F}^{*}\mathbf{QF})^{\frac{1}{2}}. \tag{4.11}$$

4.2 Linear equations for determining the kernel matrix

In the case of the designed weights $\mathbf{W}_{\mathrm{c}}$**,** the weighted data are determined by the following formula:

$$\mathbf{d}_{\mathrm{c}} = \mathbf{W}_{\mathrm{c}}\mathbf{d}, \tag{4.12}$$

or by using scalar notations,

$$\delta \mathrm{d}_{\mathrm{cj}} = \sum_{\mathrm{i}} \mathrm{w}_{\mathrm{ji}} \delta \mathrm{d}_{\mathrm{i}} = \sum_{\mathrm{i}} \mathrm{w}_{\mathrm{ji}} \mathrm{F}_{\mathrm{ik}} \delta \sigma_{\mathrm{k}}\,, \mathrm{i}, \mathrm{j} = 1,2, \ldots \mathrm{N}_{\mathrm{d}}; \mathrm{k} = 1,2, \ldots \mathrm{N}_{\mathrm{m}}; \tag{4.13}$$

where w_{ji} are the components of the designed data weighting matrix $\mathbf{W}_{\mathrm{c}}$.

The integrated sensitivity of the weighted data to the parameter $\delta\sigma_{\mathrm{k}}$ is determined, according to formula (4.1), as follows:

$$\mathrm{S}_{\mathrm{ck}} = \frac{\|\delta \mathbf{d}_{\mathrm{c}}\|}{\delta \sigma_k} = \frac{\sqrt{\sum_j \delta d_{cj}^{*} d_{cj}}}{\delta \sigma_{\mathrm{k}}} = \sqrt{\sum_i \sum_l q_{il} F_{ik}^{*} F_{lk}}, \tag{4.14}$$

where

$$\mathrm{q}_{\mathrm{il}} = \sum_{\mathrm{j}} \mathrm{w}_{\mathrm{ji}}^{*} \mathrm{w}_{\mathrm{ji}}. \tag{4.15}$$

The scalar components q_{il} form the data weighting kernel matrix **Q**,

$$\mathbf{Q} = \mathbf{W}_{\mathbf{c}}^{*}\mathbf{W}_{\mathbf{c}}, \tag{4.16}$$

where by definition:

$$\mathrm{q}_{\mathrm{il}} = \mathrm{q}_{\mathrm{li}}, \text{and } \mathrm{q}_{\mathrm{il}} = \mathrm{q}_{\mathrm{il}}^{*}. \tag{4.17}$$

Thus, we have:

$$\mathrm{S}_{\mathrm{ck}}^{2} = \sum_{\mathrm{i}}\sum_{\mathrm{l}} \mathrm{q}_{\mathrm{il}}\mathrm{F}_{\mathrm{ik}}^{*}\mathrm{F}_{\mathrm{ik}}. \tag{4.18}$$

Let us write expression (4.10) in scalar notations:

$$\sum_{\mathrm{k}}\left(\mathrm{S}_{\mathrm{ck}}^{2} - \mathrm{P}_{\mathrm{k}}^{2}\right)^{2} = \sum_{\mathrm{k}}\left(\mathrm{S}_{\mathrm{ck}}^{2} - \mathrm{P}_{\mathrm{k}}^{2}\right)^{*}\left(\mathrm{S}_{\mathrm{ck}}^{2} - \mathrm{P}_{\mathrm{k}}^{2}\right) = \min, \tag{4.19}$$

where $\mathrm{P}_{\mathrm{k}}^{2}$ are the scalar components of matrix $\mathbf{P}^{2}$.

Substituting expression (4.18) into (4.19), we have:

$$\varphi(\mathrm{q}_{\mathrm{mn}}) = \sum_{\mathrm{k}}\left(\sum_{\mathrm{i}}\sum_{\mathrm{l}} \mathrm{q}_{\mathrm{il}}\mathrm{F}_{\mathrm{ik}}^{*}\mathrm{F}_{\mathrm{ik}} - \mathrm{P}_{\mathrm{k}}^{2}\right)^{*}\left(\sum_{\mathrm{i}}\sum_{\mathrm{l}} \mathrm{q}_{\mathrm{il}}\mathrm{F}_{\mathrm{ik}}^{*}\mathrm{F}_{\mathrm{ik}} - \mathrm{P}_{\mathrm{k}}^{2}\right) = \min. \tag{4.20}$$

It is known that, at a minimum of the misfit functional $\varphi(\mathrm{q}_{\mathrm{mn}})$, its first variation $\delta_{\mathrm{qmn}}\varphi$, is equal to zero:

$$\begin{aligned}\delta_{\mathrm{qmn}}\varphi(\mathrm{q}_{\mathrm{mn}}) &= \delta_{\mathrm{qmn}}\sum_{\mathrm{k}}\left(\sum_{\mathrm{i}}\sum_{\mathrm{l}} \mathrm{q}_{\mathrm{il}}\mathrm{F}_{\mathrm{ik}}^{*}\mathrm{F}_{\mathrm{ik}} - \mathrm{P}_{\mathrm{k}}^{2}\right)^{*}\left(\sum_{\mathrm{i}}\sum_{\mathrm{l}} \mathrm{q}_{\mathrm{il}}\mathrm{F}_{\mathrm{ik}}^{*}\mathrm{F}_{\mathrm{ik}} - \mathrm{P}_{\mathrm{k}}^{2}\right)\\ &= 2\mathrm{q}_{\mathrm{mn}}\mathrm{Re}\sum_{\mathrm{k}}\left[\left(\sum_{\mathrm{i}}\sum_{\mathrm{l}} \mathrm{q}_{\mathrm{il}}\mathrm{F}_{\mathrm{ik}}^{*}\mathrm{F}_{\mathrm{ik}} - \mathrm{P}_{\mathrm{k}}^{2}\right)\mathrm{F}_{\mathrm{mk}}^{*}\mathrm{F}_{\mathrm{nk}}\right] = 0.\end{aligned} \tag{4.21}$$

In a similar way, we can find:

$$2q_{nm}\mathrm{Re}\sum_{k}\left[\left(\sum_{i}\sum_{l} q_{il}F_{ik}^{*}F_{ik} - P_{k}^{2}\right)F_{nk}^{*}F_{mk}\right] = 0. \tag{4.22}$$

Summing equations (4.21) and (4.22), and taking into account (4.17), we have:

$$\sum_{i}\sum_{l} q_{il}\,\mathrm{Re}\sum_{k} F_{ik}^{*}F_{lk}(F_{mk}^{*}F_{nk} + F_{nk}^{*}F_{mk}) = \mathrm{Re}\sum_{k} P_{k}^{2}(F_{mk}^{*}F_{nk} + F_{nk}^{*}F_{mk}). \tag{4.23}$$

Introducing the following notations,

$$\begin{gathered}\mathrm{Re}\sum_{k} F_{ik}^{*}F_{lk}(F_{mk}^{*}F_{nk} + F_{nk}^{*}F_{mk}) = a_{ilmn},\\ \mathrm{Re}\sum_{k} P_{k}^{2}(F_{mk}^{*}F_{nk} + F_{nk}^{*}F_{mk}) = b_{mn},\end{gathered} \tag{4.24}$$

we obtain the following equation:

$$\sum_{i}\sum_{l} q_{il}a_{ilmn} = b_{mn}. \tag{4.25}$$

It is clear that,

$$a_{ilmn} = a_{mnil}, a_{ilmn} = a_{limn}, a_{ilmn} = a_{ilnm}. \tag{4.26}$$

Note that, because of the symmetry of coefficients a_{ilmn} and b_{mn}, we have a symmetry of coefficients q_{il}:

$$q_{il} = q_{li}, \tag{4.27}$$

which insures that the corresponding matrix **Q** is a real and symmetrical matrix as well.

We can rewrite equation (4.23) as follows:

$$\mathbf{Aq} = \mathbf{b}, \tag{4.28}$$

where

$$\begin{gathered}\mathbf{q} = \left[\mathrm{q}_{11}, \mathrm{q}_{12}, \ldots \mathrm{q}_{1\mathrm{N}_\mathrm{d}}, q_{21} \ldots q_{N_dN_d}\right]^T, \mathbf{b} = \left[\mathrm{b}_{11}, \mathrm{b}_{12}, \ldots \mathrm{b}_{1\mathrm{N}_\mathrm{d}}, b_{21} \ldots b_{N_dN_d}\right]^T, \\ \mathbf{A} = [\mathrm{a}_{\mathrm{ilmn}}]^\mathrm{T}, \mathrm{i}, \mathrm{l}, \mathrm{m}, \mathrm{n} = 1,2, \ldots \mathrm{N}_\mathrm{d}.\end{gathered} \tag{4.29}$$

The linear equation (4.28) can be solved using Tikhonov regularization method, based on minimization of the parametric functional:

$$\mathrm{P}^\alpha(\mathbf{q}) = (\mathbf{Aq} - \mathbf{b})^\mathrm{T}(\mathbf{Aq} - \mathbf{b}) + \alpha\left(\mathbf{q} - \mathbf{q}_\mathrm{apr}\right)^\mathrm{T}\left(\mathbf{q} - \mathbf{q}_\mathrm{apr}\right) = \min, \tag{4.30}$$

where α is a regularization parameter, and $\mathbf{q}_\mathrm{apr}$ is some a priori vector of corresponding row of kernel matrix $\mathbf{Q}$. The common approach to minimization of the parametric functional $\mathrm{P}(\mathbf{m})$ is based on using gradient-type methods. We can solve this minimization problem using the regularized conjugate-gradient (RCG) method.

The algorithm of the RCG method can be summarized as follows (Zhdanov, 2002):

$$\mathbf{R}_\mathrm{n} = \mathbf{Aq}_\mathrm{n} - \mathbf{b}, \tag{4.31}$$

$$\mathbf{l}_\mathrm{n}^{\alpha_\mathrm{n}} = \mathbf{l}^{\alpha_\mathrm{n}}(\mathbf{q}_\mathrm{n}) = \mathbf{A}^\mathrm{T}\mathbf{R}_\mathrm{n} + \alpha\left(\mathbf{q}_\mathrm{n} - \mathbf{q}_\mathrm{apr}\right) \tag{4.32}$$

$$\beta_\mathrm{n}^{\alpha_\mathrm{n}} = \frac{\left\|\mathbf{l}_\mathrm{n}^{\alpha_\mathrm{n}}\right\|^2}{\left\|\mathbf{l}_{\mathrm{n}-1}^{\alpha_{\mathrm{n}-1}}\right\|^2}, \tag{4.33}$$

$$\bar{\mathbf{l}}_\mathrm{n}^{\alpha_\mathrm{n}} = \mathbf{l}_\mathrm{n}^{\alpha_\mathrm{n}} + \beta_\mathrm{n}^{\alpha_\mathrm{n}}\bar{\mathbf{l}}_{\mathrm{n}-1}^{\alpha_{\mathrm{n}-1}}, \tag{4.34}$$

$$\bar{\mathbf{I}}_0^{\alpha_0} = \mathbf{I}_0^{\alpha_0}, \tag{4.35}$$

$$\tilde{\mathrm{k}}_{\mathrm{n}}^{\alpha_{\mathrm{n}}} = \frac{\bar{\mathbf{I}}_{\mathrm{n}}^{\alpha_{\mathrm{n}}\,T}\mathbf{I}_{\mathrm{n}}^{\alpha_{\mathrm{n}}}}{\left(\mathbf{A}\bar{\mathbf{I}}_{\mathrm{n}}^{\alpha_{\mathrm{n}}}\right)^T\left(\mathbf{A}\bar{\mathbf{I}}_{\mathrm{n}}^{\alpha_{\mathrm{n}}}\right) + \alpha\left(\bar{\mathbf{I}}_{\mathrm{n}}^{\alpha_{\mathrm{n}}\,T}\bar{\mathbf{I}}_{\mathrm{n}}^{\alpha_{\mathrm{n}}}\right)} \tag{4.36}$$

$$\mathbf{q}_{\mathrm{n}+1} = \mathbf{q}_{\mathrm{n}} - \tilde{\mathrm{k}}_{\mathrm{n}}^{\alpha_{\mathrm{n}}}\,\bar{\mathbf{I}}_{\mathrm{n}}^{\alpha_{\mathrm{n}}}, \tag{4.37}$$

where $\tilde{\mathrm{k}}_{\mathrm{n}}^{\alpha_{\mathrm{n}}}$ is the step length, $\mathbf{I}_{\mathrm{n}}^{\alpha_{\mathrm{n}}}$ is the gradient direction computed using a transposed matrix, $\mathbf{A}^{\mathrm{T}}$, and α_{n} are the subsequent values of the regularization parameter. The above inversion method is called an RCG scheme with adaptive regularization. In the framework of this iterative approach, we begin the initial iteration without regularization $(\alpha_0 = 0)$. We apply the regularization in the next step. The first value of the regularization parameter, α_1, is determined after the initial iteration, as ratio:

$$\alpha_1 = \frac{\|\mathbf{A}(\mathbf{q}_0) - \mathbf{b}\|^2}{\|\mathbf{q}_0\|^2}. \tag{4.38}$$

This selection of α_1 provides a balance between the misfit and stabilizing functionals. For any subsequent iteration, we update the value of the regularization parameter α_{k} according to the following progression:

$$\alpha_{\mathrm{k}} = \alpha_1 q^{\mathrm{k}-1}, \mathrm{k} = 1,2,\dots,\mathrm{n}; 0 < q < 1. \tag{4.39}$$

The iterative inversion is terminated when the misfit condition is reached:

$$\varphi(\boldsymbol{q}_{\mathrm{k}0}) = (\mathbf{A}(\mathbf{q}_{\mathrm{k}0}) - \mathbf{b})^{\mathrm{T}}(\mathbf{A}(\mathbf{q}_{\mathrm{k}0}) - \mathbf{b}) = \delta^2. \tag{4.40}$$

The solution of the RCG method, vector $\boldsymbol{q}$,

$$\mathbf{q} = \left[\mathrm{q}_{11}, \mathrm{q}_{12}, \dots \mathrm{q}_{1\mathrm{N_d}}, q_{21} \dots q_{N_d N_d}\right]^T, \mathbf{b} = \left[\mathrm{b}_{11}, \mathrm{b}_{12}, \dots \mathrm{b}_{1\mathrm{N_d}}, b_{21} \dots b_{N_d N_d}\right]^T, \qquad (4.41)$$

is used to define the data weighting kernel matrix $\boldsymbol{Q} = [\mathrm{q}_{\mathrm{il}}]$.

CHAPTER 5

NUMERICAL STUDY OF 1D CONTROLLED SENSITIVITY

5.1 Survey design for 1D controlled sensitivity

We illustrate the application of the described method for computing the 1D controlled sensitivities for several case studies. The typical MCSEM survey is formed by a set of sea bottom electrical and magnetic receivers and a horizontal electric dipole transmitter towed at some elevation above the sea bottom. We consider a simple basic survey, consisting of just one receiver and an electric dipole transmitter moving above this receiver in the x direction along a 14 km line at an elevation of 50 m above the sea bottom (Figure 5.1). The transmitter generates a frequency domain EM field with a frequency of 0.1 Hz from the points located every 500 m along the transmitter line. Later, we will use different frequencies for analysis of the controlled sensitivity. The maximum and minimum transmitter-receiver offsets are 7 km and 1 km, respectively. A single receiver is located at the sea floor and measures the E_x component of the electric field and the H_y component of the magnetic field. The background geoelectric model consists of a seawater layer with a thickness of 500 m, a resistivity of 0.25 Ohm-m, and a layer of conductive sea bottom sediments with a resistivity of 1 Ohm-m. The domain for our sensitivity study extends from 1000 m to 2000 m in depth

5.2 1D integrated sensitivities of the basic MCSEM survey

In order to understand the concepts of the integrated sensitivity and the weighted integrated sensitivity, we compute these sensitivities for the basic survey design described in Figure 5.1. Figures 5.2 and 5.3 present the plots of the original integrated sensitivities for this basic survey (shown by the red dashed lines). We can see that the integrated sensitivities for both electric and magnetic field components decrease rapidly with the depth, indicating that the survey data are mostly sensitive to the upper layers of the sea bottom formations. Those figures also present plots of the weighted integrated sensitivities (shown by the blue dashed lines). Note that, in order to be able to compare these two sensitivity distribution, we have plotted the sensitivities normalized by their maximum value. One can see that the application of the data weights increases the integrated sensitivity of the survey significantly. That is why data weighting is important in MCSEM data interpretation.

5.3 Selection of the 1D a priori sensitivity

As we discussed in Chapter 4, we select *a priori sensitivity* **P** based on the estimated depth of the reservoir. Theoretically, we can select any form for an a priori sensitivity, but practically, we have to select a physically realizable form; otherwise it would be computationally difficult to find a desired controlled sensitivity that would satisfy equation (4.1).

For the 1D controlled sensitivity, we will consider three types of a priori sensitivities. First, in Model 1 we simply construct the a priori sensitivity using the maximum and minimum values of the original integrated sensitivity for both the x component of the electric field, E_x, and for the y component of the magnetic field, H_y. We set the maximum value for the a priori sensitivity within the target area ranging from 1150 m to 1400 m, and assign the minimum value for the sensitivity to other depths for both electric and magnetic fields (Figure 5.4). We construct the a priori sensitivity of Model 1 for the magnetic field component, H_y, in the same way as for the electric field component, E_x.

In Model 2, we keep the same target area, but increase the minimum value of the a priori sensitivity of Model 1.

Lastly, in Model 3 we use the same maximum and minimum values of the a priori sensitivity as in Model 2, but locate the target area at a depth ranging from 1450 m to 1800 m. Note that, in graphical representations of the a priori and controlled sensitivities, we plot the corresponding values normalized by the maximum of the original sensitivity.

5.4 Determining 1D controlled sensitivity by inversion

We have applied an inversion method, described in section 4.2, in order to find the controlled sensitivity according to equation (4.1). We will analyze the results using three different types of models. All of these models are based on the simple basic survey design, presented in Figure 5.1. The difference among the models is the manner in which the a prior sensitivity is selected. We also consider the controlled sensitivities computed for the E_x or H_y components, and for different frequencies.

5.4.1 1D controlled sensitivity for Model 1

As mentioned in the previous section, we use the maximum and the minimum values of the original sensitivity to design the a priori sensitivity for Model 1. The target area is located in the depth interval ranging from 1150 m to 1400 m.

Figure 5.4 shows an inversion result for the controlled sensitivity of the E_x component, at a frequency of 0.1 Hz. From this figure, we can see that the original sensitivity (red dashed line) decreases rapidly with the depth. After applying the data weighting kernel matrix **Q**, which is determined from solving the minimization problem (4.10), and calculating the corresponding controlled sensitivity using equation (4.11), we can see that the obtained controlled sensitivity (black dashed line) corresponds well to the a priori preselected sensitivity (solid line), increasing the sensitivity in the target area. The sensitivity plots for the magnetic component have similar behavior, as can be seen in Figure 5.5.

5.4.2 1D controlled sensitivity for Model 2

In Model 2, we have slightly modified the a priori sensitivity by using half the maximum of the original integrated sensitivity in the depth intervals outside the target area. Figure 5.6 shows the plots of the a priori, original, and controlled integrated sensitivities normalized by the maximum of the original sensitivity. The sensitivities are computed for the electric field component, E_x, at a frequency of 0.1 Hz. One can see a very good representation by the controlled sensitivity of the designed a priori resistivity.

In the next set of numerical experiments, we calculate the corresponding controlled sensitivities for cases of both the E_x and H_y components for a number of decreasing frequencies, from 0.75 Hz to 0.01 Hz (Figures 5.7 and 5.8), in order to analyze controlled sensitivity distributions computed with different frequencies. From there results, we can see that the obtained controlled sensitivity curves represent well the a priori selected sensitivity, providing the maximum sensitivity within the target area. Also, we can see that the curve with a higher frequency increases more within the target area and decreases outside of the target area. Therefore, higher frequency more effectively controls the sensitivity, if the target area is located within a relatively shallow depth interval. Note that, for every frequency, the linear system of equations (4.28) was iteratively solved for a 1% level of misfit, as shown in Figure 5.9.

We can also calculate the controlled sensitivity for multifrequency data. Figure 5.10 presents a plot of the controlled sensitivity calculated for two frequencies of 0.25 Hz and 0.1 Hz for the electric, E_x, and magnetic, H_y, components, respectively. One can see that the result is improved, when we use multifrequency data in comparison with single-frequency controlled sensitivity.

5.4.3 1D controlled sensitivity for Model 3

Finally, we consider Model 3 with the target area located at a depth ranging from 1450 m to 1800 m, and calculate the corresponding controlled sensitivity for the E_x and H_y components, using different frequencies ranging from 0.75 to 0.01 Hz.

Figure 5.11 shows the controlled sensitivities of the E_x components for the frequencies 0.75, 0.25, 0.1 and 0.01 Hz. One can see that the peak points of the obtained sensitivity curves are getting closer to those of the target area, as the frequency gets lower. The skin depth of an electromagnetic field with the higher frequency is larger than for a lower frequency. Physically, it is easier to control the sensitivity by using the lower frequency if the target area is located at a relatively deeper depth interval. We calculate the controlled sensitivity for the H_y component with a number of decreased frequencies from 0.75 Hz to 0.01 Hz (Figure 5.12).

Finally, we present in Figure 5.13 the plots of the controlled sensitivity calculated for Model 3 using two frequencies of 0.25 Hz and 0.1 Hz for the electric, E_x, and magnetic, H_y, components, respectively. One can see that the result is improved over those obtained for a singular frequency.

5.4.4 Characteristics of the data weighting kernel matrix Q

The maps of the corresponding matrices **Q** for Model 2, computed for the electric field component, E_x, at the frequencies of 0.75, 0.25, 0.1, and 0.01 Hz, are shown in Figures 5.14, 5.15, 5.16 and 5.17, respectively. One can clearly see the symmetric structure of matrix **Q** in these images. Also, we observe an oscillating "radiating" pattern of matrix **Q** composed of the real positive and negative values. This pattern indicates that the application of this matrix to the observed data may result in the artificial interference of the fields produced by the transmitters in different locations, computed according to formula (4.5). The matrix changes the magnitude and the phase of the EM signal, unlike the diagonal matrix of data weights $\mathbf{W}_d$ that changes only their magnitude. This property of matrix **Q** will be discussed in section 6.4.5 as well.

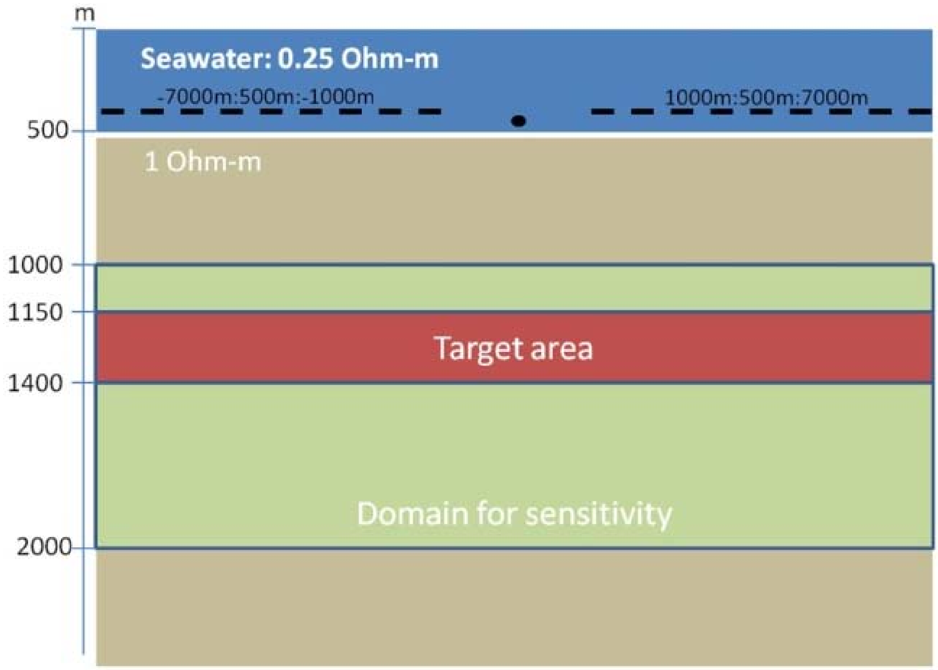

Figure 5.1. A sketch of a simple basic survey design consisting of just one receiver and an electric dipole transmitter moving above this receiver in the x direction along a 14 km line with 500 m distance between transmitter points at an elevation of 50 m above the sea floor.

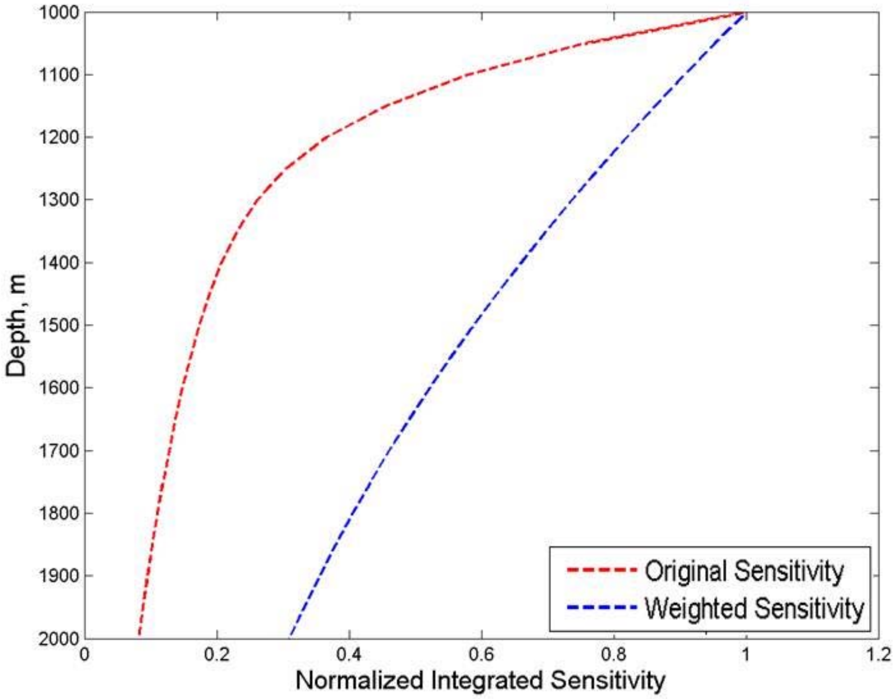

Figure 5.2. Plots of the original and weighted integrated sensitivities normalized by the corresponding maximum values. The sensitivities are computed for the electric field component, E_x, at a frequency of 0.1 Hz.

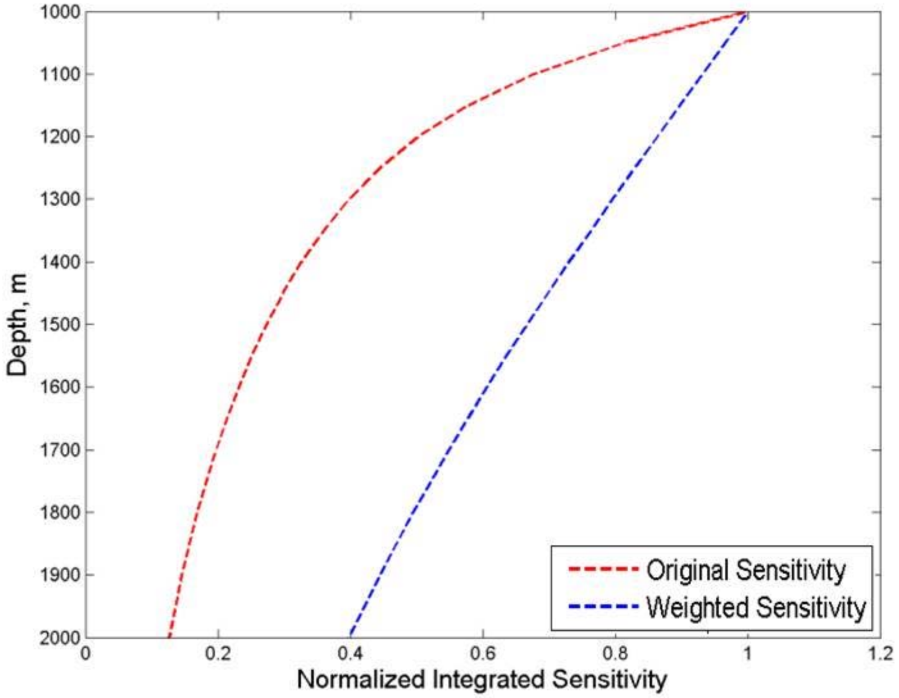

Figure 5.3. Plots of the original and weighted integrated sensitivities normalized by the corresponding maximum values. The sensitivities are computed for the magnetic field component, H_y, at a frequency of 0.1 Hz.

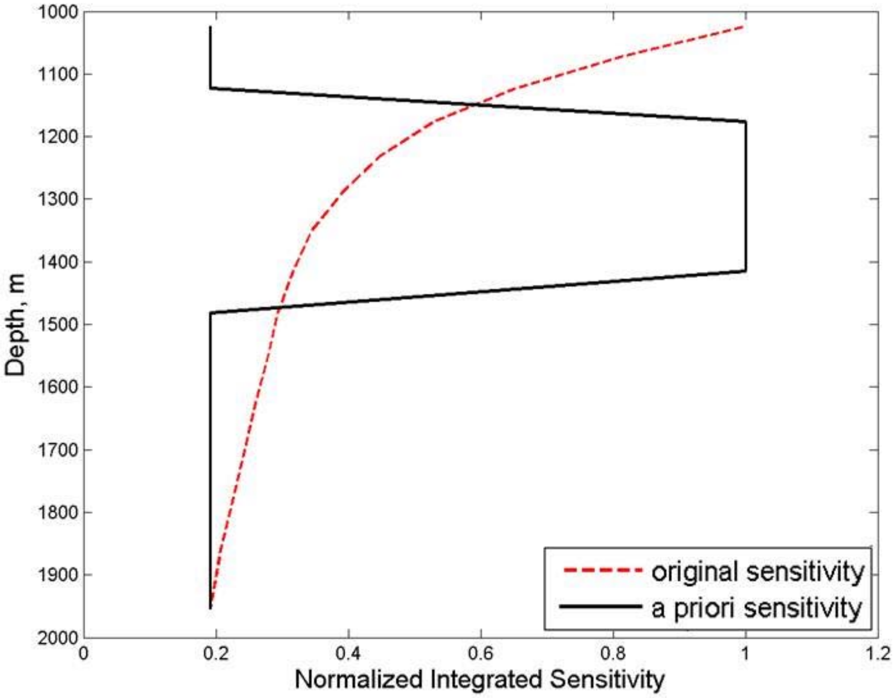

Figure 5.4. Model 1. Plots of the original and a priori sensitivities normalized by the maximum value of the original sensitivity. The sensitivities are computed for the electric field component, E_x, at a frequency of 0.1 Hz.

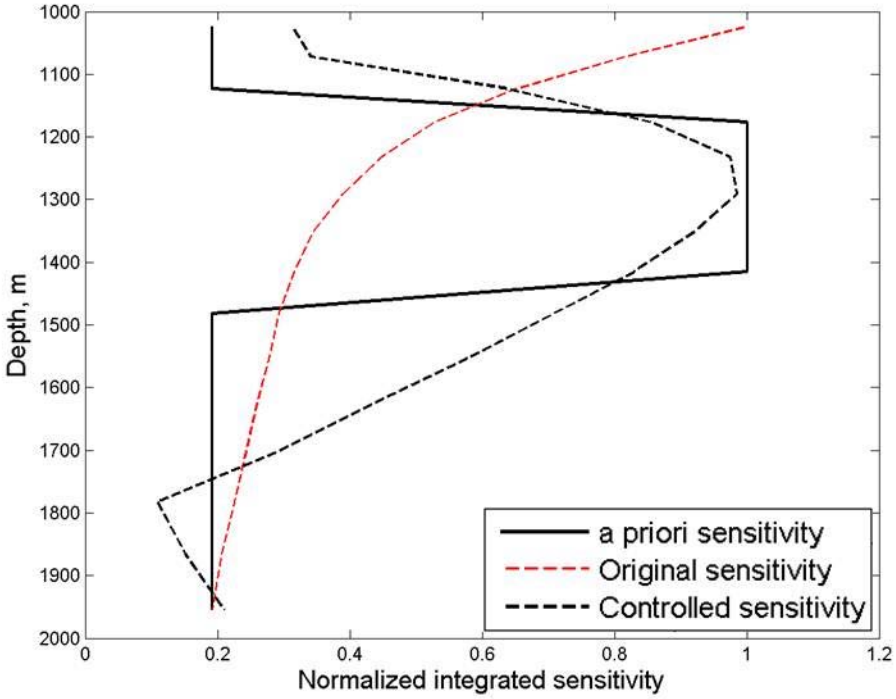

Figure 5.5. Model 1. Plots of the a priori, original, and controlled integrated sensitivities, normalized by the maximum value of the original sensitivity. The sensitivities are computed for the electric field component, E_x, at a frequency of 0.1 Hz.

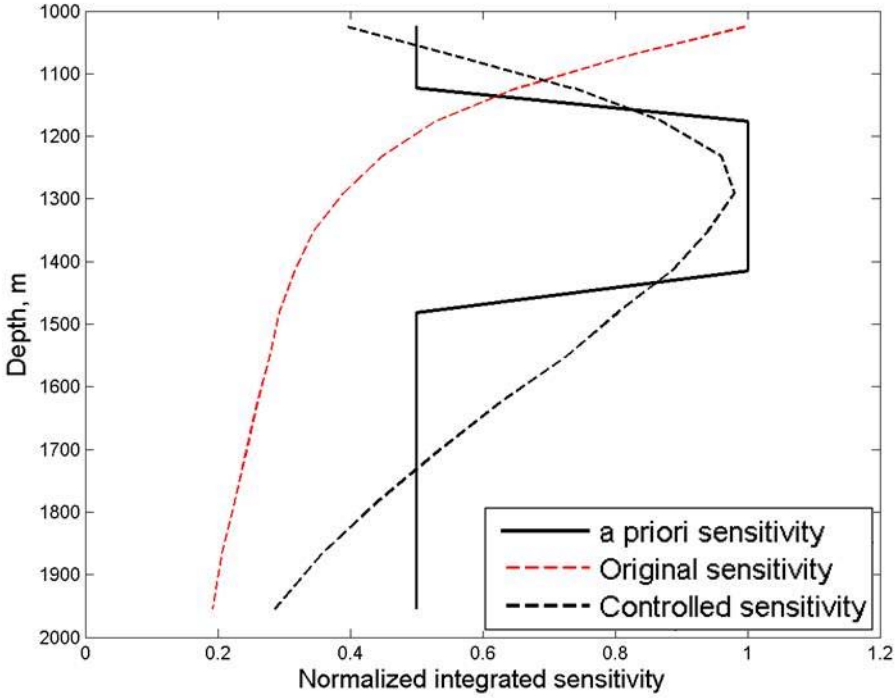

Figure 5.6. Model 2. Plots of the a priori, original, and controlled integrated sensitivities, normalized by the maximum value of the original sensitivity. The sensitivities are computed for the electric field component, E_x, at a frequency of 0.1 Hz.

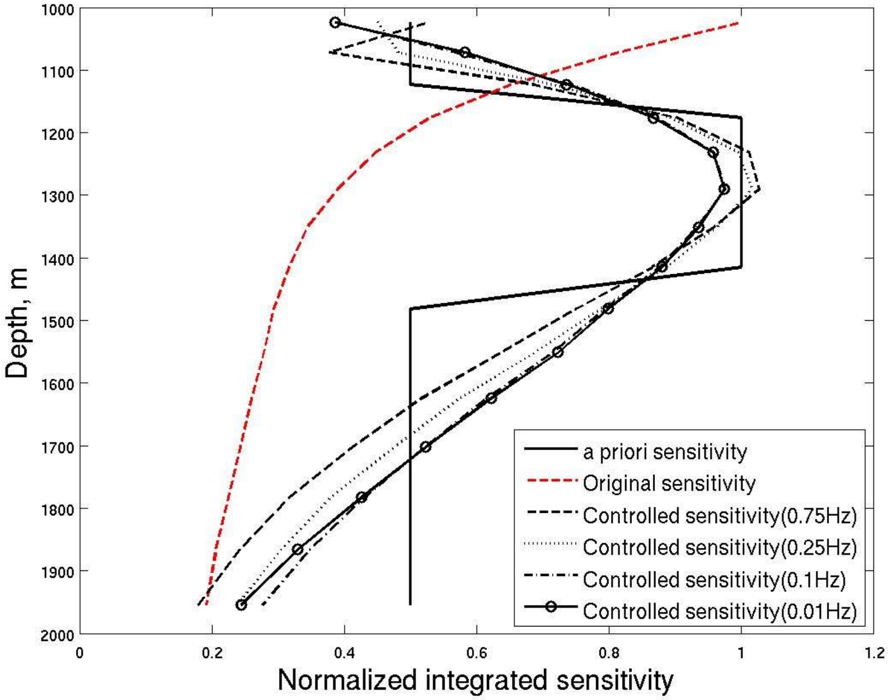

Figure 5.7. Model 2. Plots of the a priori, original, and controlled integrated sensitivities normalized by the maximum value of the original sensitivity. The sensitivities are computed for the electric field component, E_x, at the frequencies of 0.75, 0.25, 0.1, and 0.01 Hz.

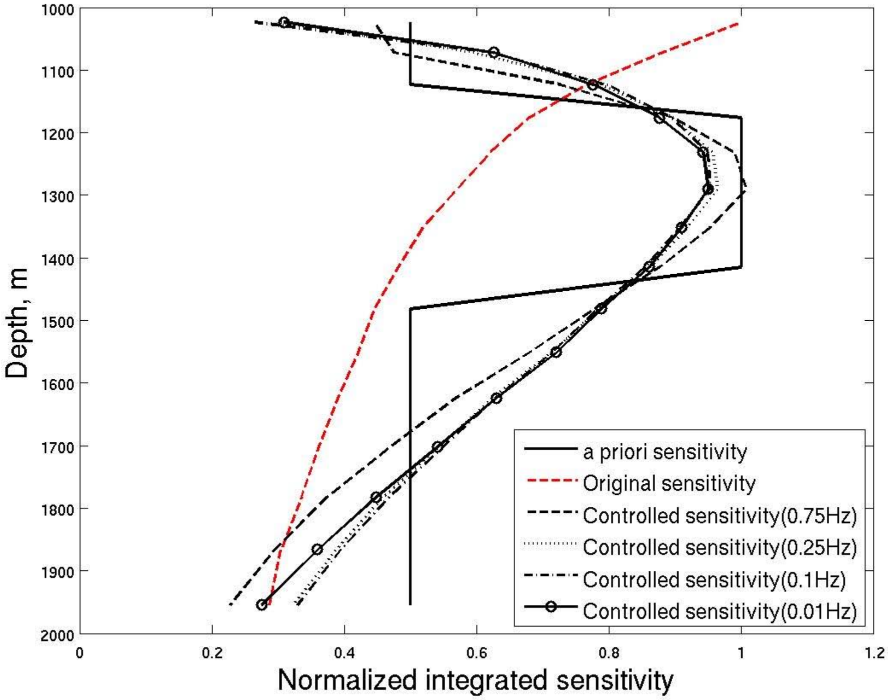

Figure 5.8. Model 2. Plots of the a priori, original and controlled integrated sensitivities normalized by the maximum value of the original sensitivity. The sensitivities are computed for the magnetic field component, H_y, at the frequencies of 0.75, 0.25, 0.1, and 0.01 Hz.

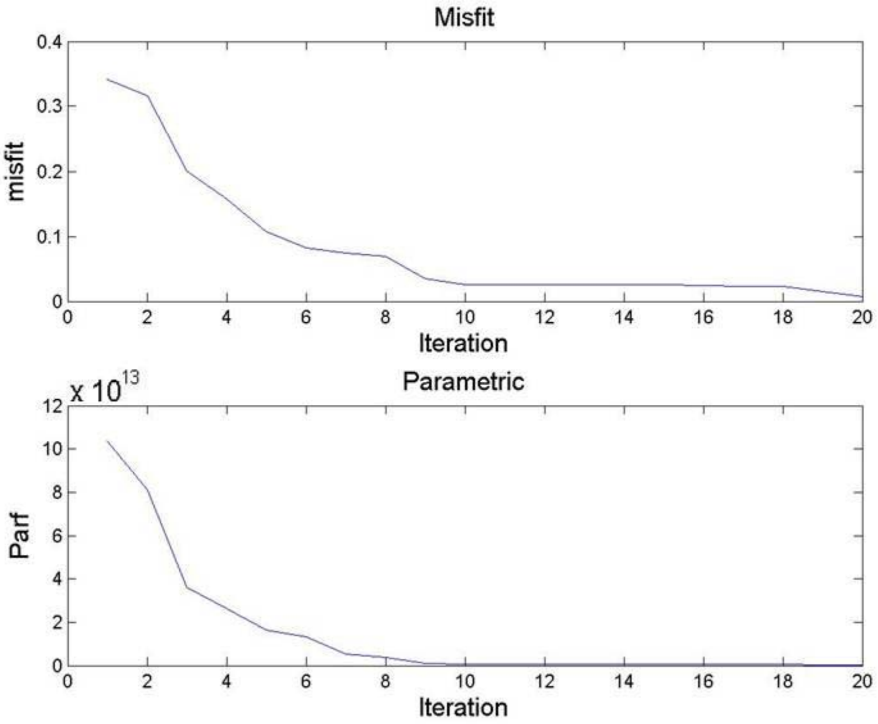

Figure 5.9. Plots of the misfit and parametric functionals versus iteration number in the inversion for the controlled integrated sensitivity for E_x component at a frequency of 0.1 Hz.

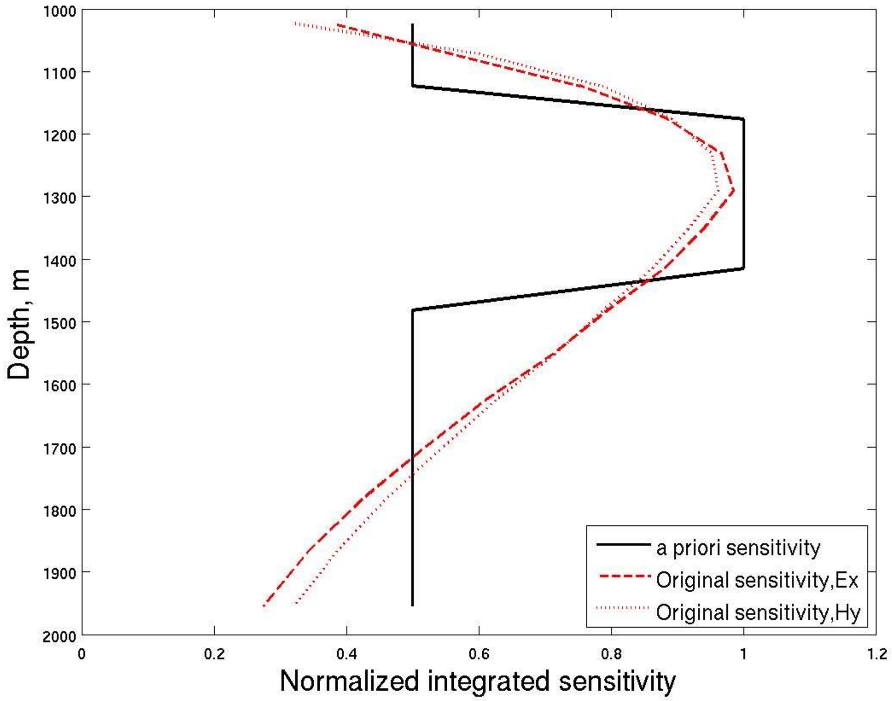

Figure 5.10. Model 2. Plots of the a priori, original and controlled integrated sensitivities normalized by the maximum value of the original sensitivity. The sensitivities are computed for two frequencies of 0.25 and 0.1 Hz for the electric, E_x, and magnetic, H_y, components, respectively.

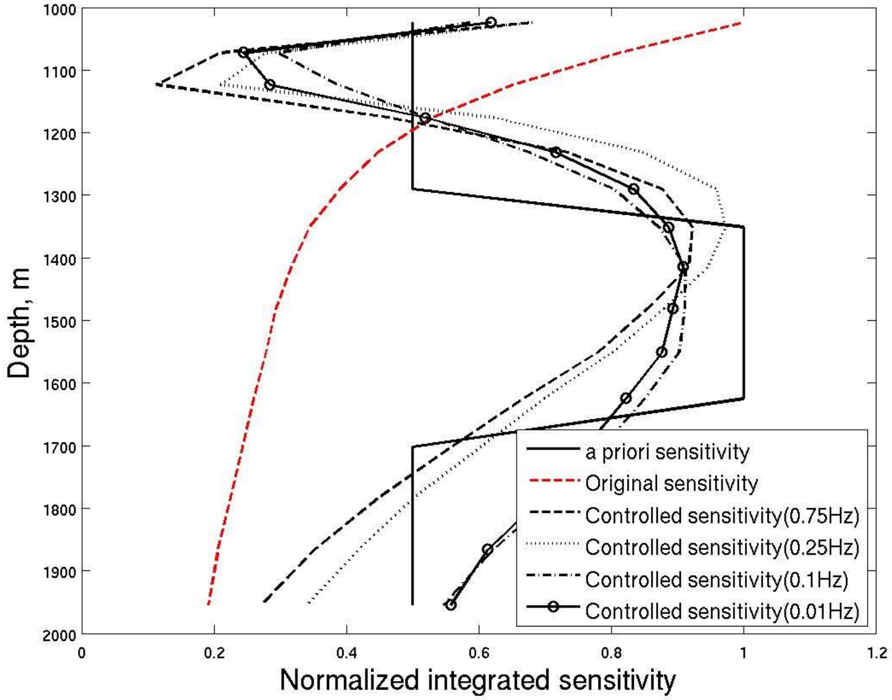

Figure 5.11. Model 3. Plots of the a priori, original, and controlled integrated sensitivities, normalized by the maximum value of the original sensitivity. The sensitivities are computed for the electric field component, E_x, at frequencies of 0.75, 0.25, 0.1, and 0.01 Hz.

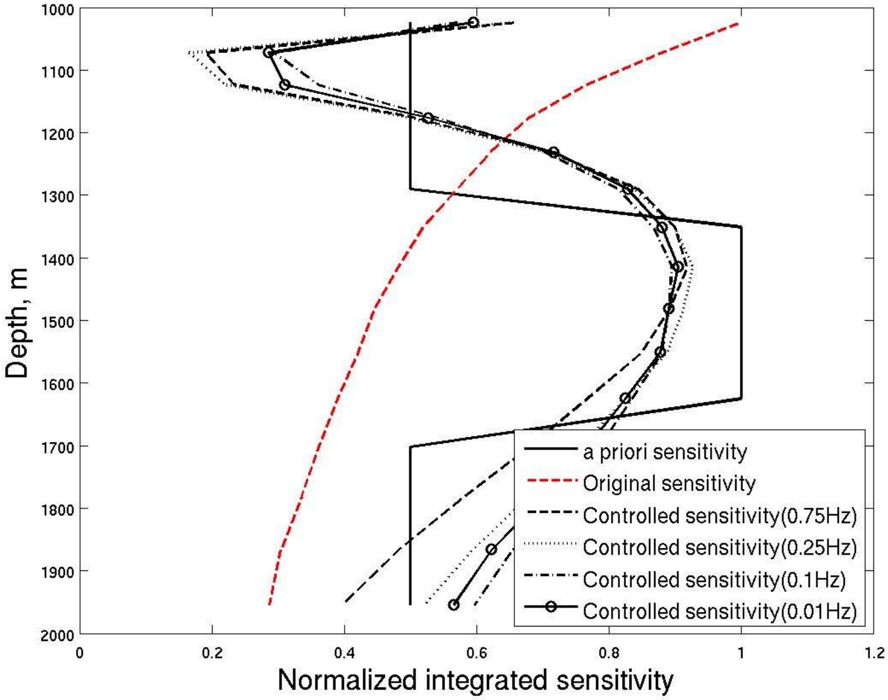

Figure 5.12. Model 3. Plots of the a priori, original, and controlled integrated sensitivities, normalized by the maximum value of the original sensitivity. The sensitivities are computed for the magnetic field component, H_y, at frequencies of 0.75, 0.25, 0.1, and 0.01 Hz.

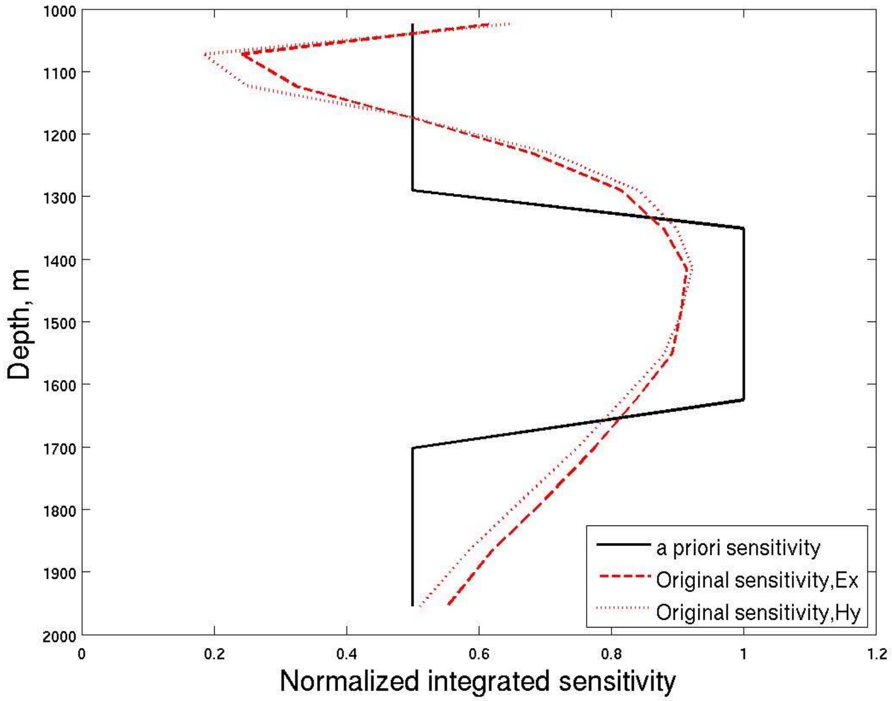

Figure 5.13. Model 3. Plots of the a priori, original, and controlled integrated sensitivities, normalized by the maximum value of the original sensitivity. The sensitivities are computed for two frequencies of 0.25 and 0.1 Hz for the electric, E_x, and magnetic, H_y, components, respectively.

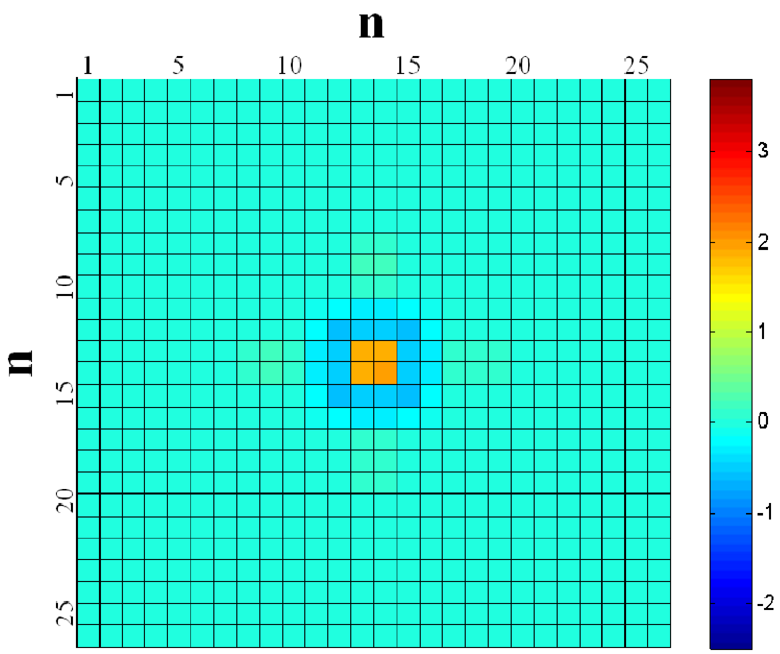

Figure 5.14. A map of matrix Q for Model 2, computed for electric field component, , at a frequency of 0.75 Hz.

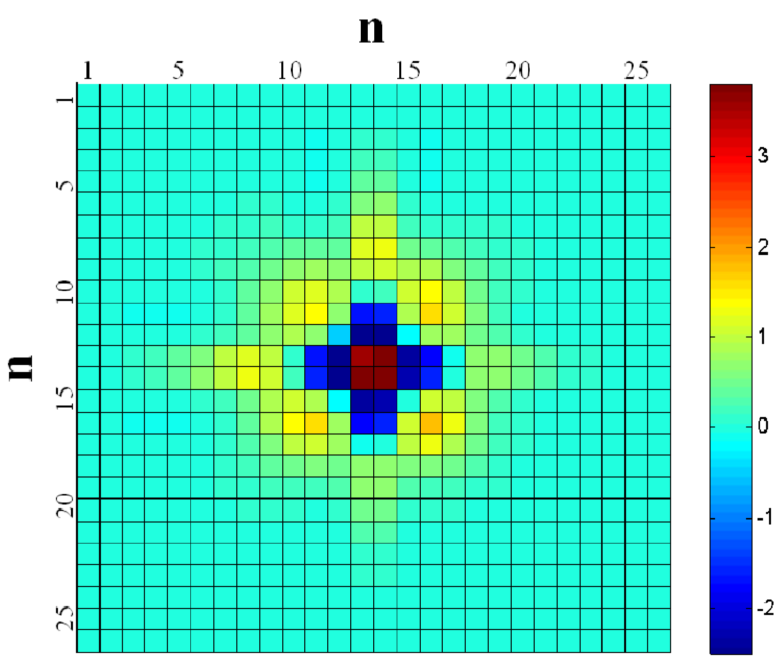

Figure 5.15. A map of matrix Q for Model 2, computed for electric field component, , at a frequency of 0.25 Hz.

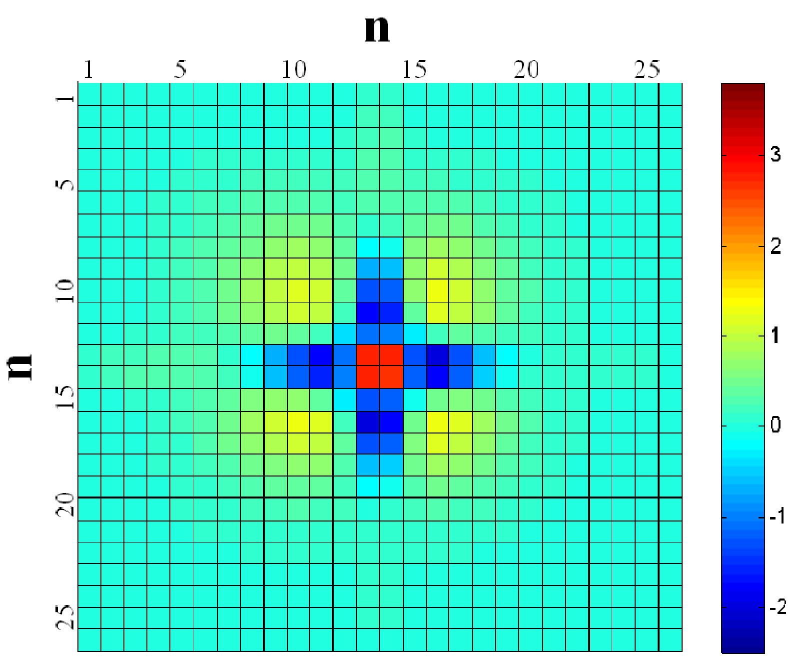

Figure 5.16. A map of matrix Q for Model 2, computed for electric field component, , at a frequency of 0.1 Hz.

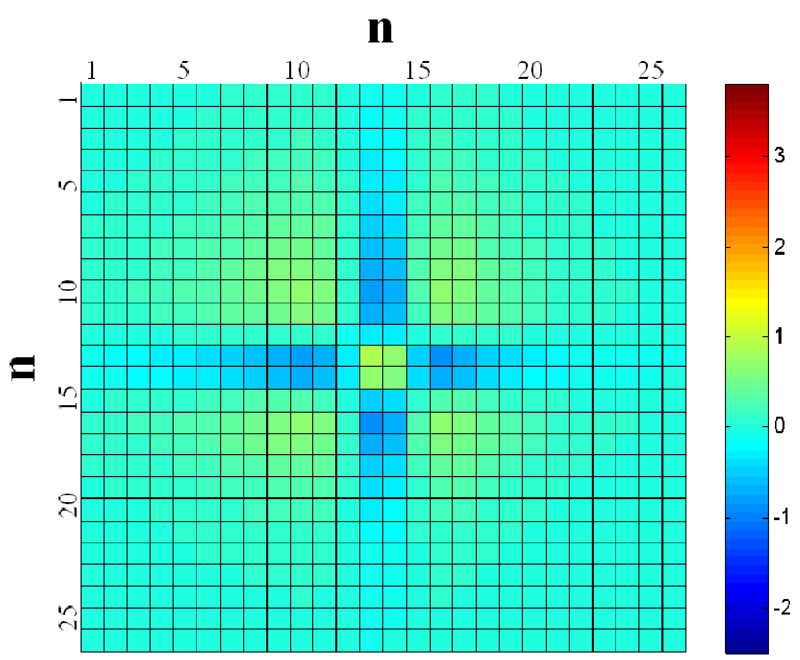

Figure 5.17. A map of matrix Q for Model 2, computed for electric field component, , at a frequency of 0.01 Hz.

CHAPTER 6

NUMERICAL STUDY OF 2D CONTROLLED SENSITIVITY

6.1 Survey design for 2D controlled sensitivity

In the previous chapter, we have shown the application of the developed method for computing 1D controlled sensitivity. In this chapter, we extend the method to compute 2D controlled sensitivity. We still consider a simple basic MCSEM survey design similar to one shown in Figure 5.1. However we consider the survey with not only one receiver, but also with three receivers, as shown in Figure 6.1. Those receivers are located at the sea floor and measure the E_x component of the electric field and the H_y component of the magnetic field. An electric dipole transmitter is moving above the receivers in the x direction along a 14 km line at an elevation of 50 m above the sea bottom. The transmitter generates a frequency domain EM field with a frequency of 0.1 Hz from the points located every 500 m along the transmitter line. We will also use different frequencies in order to analyze the effect of the frequency on the controlled sensitivity. The maximum and minimum transmitter-receiver offsets are 7 km and 1 km, respectively. The background geoelectric model consists of a seawater layer with a thickness of 500 m, and a resistivity of 0.25 Ohm-m, and a layer of conductive sea bottom sediments with a resistivity of 1 Ohm-m. The domain of the sensitivity study extends from 1000 m to 2000 m in depth.

6.2 2D integrated sensitivities for the basic MCSEM survey

Using a simple basic survey design presented in Figure 6.1, we compute the original and the weighted integrated sensitivities for the E_x component of the electric field and the H_y component of the magnetic field.

Figure 6.2 presents the plots of the original integrated sensitivity (the top panel) and the weighted integrated sensitivity (the bottom panel) for the basic survey design with only one receiver, computed for the E_x component, and at a frequency of 0.1 Hz. Both sensitivities are normalized to their maximum values.

Without data weighting, the original integrated sensitivity decreases rapidly with the depth, indicating that the survey data are mostly sensitive to the conductivity in the vicinity of the receiver location only, as one can see in the top panel of Figure 6.2. With data weighting, one can see from the bottom panel in Figure 6.2 that the integrated sensitivity increases in a large area away from the receiver. Figure 6.3 presents the sensitivity distributions computed for a survey with three receivers for the E_x component and a frequency of 0.1 Hz.

In this case, the survey data are more sensitive to the conductivity variations than for one receiver only. From these experiments, we conclude that using more receivers makes it easier for us to control the sensitivity because the data obtained from multiple receivers are more sensitive to the sea bottom conductivity. The sensitivity plots for the magnetic component have similar behavior, as one can see in Figures 6.2 and 6.3.

6.3 Selection of the a priori sensitivity

In the case of 2D controlled sensitivity, we construct four types of models for a priori sensitivities for both the x component of the electric field, E_x and the y component of the magnetic field, H_y:

1) Model 1 - horizontally extended target area in the shallow layer of the sea bottom formation.

2) Model 2 - vertically extended target area.

3) Model 3 - box shaped target area.

4) Model 4 - horizontally extended target area in the deep layer of the sea bottom formation.

We set the maximum value of the original sensitivity within the target area, and assign the minimum value of the sensitivity to surrounding areas for both electric and magnetic fields.

6.4 Determining 2D controlled sensitivity by inversion

In this section we present the results of computing the 2D controlled sensitivity for four models. In each model, we consider the effects of the frequencies, and the number of receivers.

6.4.1 2D controlled sensitivity for Model 1

In the case of Model 1, we construct a simple a priori sensitivity, whose target area is extended horizontally at a relatively shallow depth interval ranging from 1200 m to 1400 m. We present only one example of a priori sensitivity computed for the E_x component at a frequency of 0.1 Hz (Figure 6.4).

Figure 6.5 shows the 2D controlled sensitivity computed for the survey with one receiver, measuring the E_x component, at a frequency of 0.1 Hz. The white outline box in this figure indicates the location of the target area. Comparing this result with the original sensitivity distribution, presented in Figure 6.2, one can see that the part with high sensitivity is moved from the vicinity of the receiver location to within the target area. This result proves that the sensitivity can be controlled by applying the data weighting kernel matrix **Q** to the survey data, focusing the sensitivity with respect to the target area.

In the next example, we compute the controlled sensitivity with the same parameters as above, but changing the frequency from 0.1 Hz to 0.01 Hz (Figure 6.6). One can see that the obtained controlled sensitivity distribution represents well the a priori sensitivity, increasing the sensitivity within the target area.

In addition, the sensitivity becomes broader and deeper, but the maximum sensitivity decreases in comparison with 0.1 Hz (Figure 6.6). This phenomenon is related to the skin depth effect, as explained above.

We can also calculate the controlled sensitivity for multiple receivers. Figures 6.7 and 6.8 present the plots of controlled sensitivity computed for three receivers at a frequency of 0.1 Hz for the electric, E_x, and the magnetic, H_y, components, respectively. We can see that the results are improved over those obtained for one receiver. Note that the sensitivity distributions are normalized by the maximum of the corresponding a priori sensitivities.

6.4.2 2D controlled sensitivity for Model 2

In the case of Model 2, a priori sensitivity has a vertical target area ranging from 1000 m to 3000 m in the x direction as shown in Figure 6.9.

Figures 6.10 and 6.11 present the controlled sensitivity distributions computed for the E_x component, at a frequency of 0.1 Hz, and for one receiver and three receivers, respectively. Both figures show very good results increasing the sensitivities within the target area. One can also see that the result is improved, when we use three receivers instead of only one, as they controlled sensitivity focused more on the target area. We also calculate the controlled sensitivity for the H_y component, three receivers, and a frequency of 0.1 Hz as shown in Figure 6.12. One can see that the controlled sensitivity increases in the target area as well.

6.4.3 2D controlled sensitivity for Model 3

We now construct a priori sensitivity with the box shaped target area, ranging from 1000 m to 2000 m in the x direction and from 1200 m to 1400 m in the depth (Figure 6.13). This target area is produced by an overlap between the target areas of Model 1 and Model 2. Figures 6.14 and 6.15 present the controlled sensitivities obtained for the $E_x$and the H_y components, respectively. The sensitivities are computed for three receivers at a frequency of 0.1 Hz. Both figures also show good results, placing the maximum values of the sensitivities within the target areas.

6.4.4 2D controlled sensitivity for Model 4

In the case of final Models, we locate the target area horizontally in the deeper layer than one of Model 1, ranging from 1500 m to 1700 m in the depth as shown in Figure 6.16.

We compute the controlled sensitivity for the E_x component, three receivers, at the frequencies of 0.1 and 0.01 Hz, as shown in Figures 6.17 and 6.18, respectively. As we have expected from the study with a similar situation of the 1D controlled sensitivity in section 5.4.3, both sensitivity distributions show improved results in comparison with the original sensitivity. When we compare those two results, we can see that the sensitivity with lower frequency is broader and deeper than that with higher frequency. Also we can see that as the frequency decreases, the maximum of the obtained sensitivity shifts down towards the target area.

6.4.5 Characteristics of the data weighting kernel matrix Q

In section 5.4.4, we have analysed the data weighting kernel matrix **Q** for 1D controlled sensitivity. In this section, we will illustrate matrix **Q** for 2D controlled sensitivity based on the survey with three receivers. If the survey has multiple transmitters and receivers, matrix **Q** becomes more complicated increasing in size proportional to the number of data. To understand better how matrix **Q** affects the data, it would be necessary to analyze not only matrix **Q** but also the weighted data $\mathbf{d}_w$ as well.

Figures 6.20 through 6.23 present the maps of matrices **Q** computed for different a priori sensitivities for Model 1 through Model 4, respectively. All maps are plotted for the E_x component at a frequency of 0.1 Hz, and a survey with 3 receivers and 26 transmitter points as shown in Figure 6.1. As the number of data is now 78, the vector of the observed data can be represented as

$$\mathbf{d} = (d_1, \dots, d_{26}, d_{27}, \dots, d_{52}, \dots, d_{78})^{\mathrm{T}},$$

Note that the data are arranged in the order of receiver and then transmitter based on the reciprocity principle. So, the first 26 components indicate the data obtained from the first receiver and the all sets of transmitter, and so on. For convenience, we number the receivers in the increasing order in the x direction shown in Figure 6.1. According to the matrix notation of the matrix **Q** in equation (4.29), the application of the matrix **Q** to data generates the weighted data:

$$\mathbf{d}_{\mathrm{w}^*w} = (d_{\mathrm{w}^*w1}, \dots, d_{\mathrm{w}^*w26}, d_{\mathrm{w}^*w27}, \dots, d_{\mathrm{w}^*w52}, \dots, d_{\mathrm{w}^*w78})^{\mathrm{T}},$$

where the components of the weighted data (d_{w^*wi}) are

$$d_{\mathrm{w}^*wi} = \sum_{j=1}^{78} q_{ij} d_j \, , i = 1,2, \dots ,78.$$

One can see that the weighted data are superposed by all set of the transmitter as well as the receivers.

Each matrix **Q** in Figures 6.19 through 6.22 can be divided into 9 small sections with a size of 26 × 26 depending on the number of receivers, and we call them section A ~ I, as denoted in Figure 6.19. One can see that each section also shows the radiating and oscillating pattern as shown in the maps of the 1D case. Also, when we apply matrix **Q** to the data, we can see that a set of the data related to one receiver is affected by only one column set of the sections of the matrix **Q**. For example, the data set from the first receiver $(d_1, \dots, d_{26})^{\mathrm{T}}$ is multiplied by sections A, D and G only.

Let us compare the maps of matrices **Q** for Model 1 and 4, which are computed for shallow and deep horizontal target areas, respectively (Figures 6.19 and 6.22). First, those matrices are symmetric about their centers, which are called centrosymmetric matrices. Those results are in agreement with the fact that the corresponding survey geometries, including locations of transmitters, receivers and target area, are designed symmetrically along the vertical line with the receiver in the center. Also, both matrices are more weighted in the diagonal sections, which means they are more focused on the data set related to the one receiver. For example, matrix **Q** gives more weights to the data observed by the first receiver, in order to generate the corresponded weighted data with the same receiver set. The difference between Figures 6.19 and 6.22 is that the matrix **Q** for Model 1 is more weighted and focused in the center of each section than that for Model 4. We can also conclude that the matrix **Q** emphasizes the data with short transmitter - receiver offsets in the case of the sensitivity focused on the shallow area. This behavior agrees well with the fact that the depth of low frequency (almost DC current) propagation is proportional to the transmitter – receiver offset.

Similar behavior is observed in Figures 6.20 and 6.21, which are computed for the target areas located on the right side of the receivers. First, matrices provide more weights in the right side and in the bottom of the area of investigation. Also, one can see that the sensitivity for Model 2 (Figure 6.12) is more focused in the subsurface in comparison to those for Model 3 (Figure 6.15). This difference makes matrix **Q** for Model 2 more weighted and focused in the center of the corresponding section.

Figure 6.23 presents an example of the application of matrix $\mathbf{Q}$ (Figure 6.20) to the observed data. The top panel shows the magnitude of the E_x component of the electric field observed in the center receiver. The bottom panel presents the weighted data, $\mathbf{d}_{w^*w} = \mathbf{Qd}$. One can see that, after applying matrix $\mathbf{Q}$ to data $\mathbf{d}$, the observed signal is shifted toward the target area, which is located from 1000 m to 3000 m in the x direction.

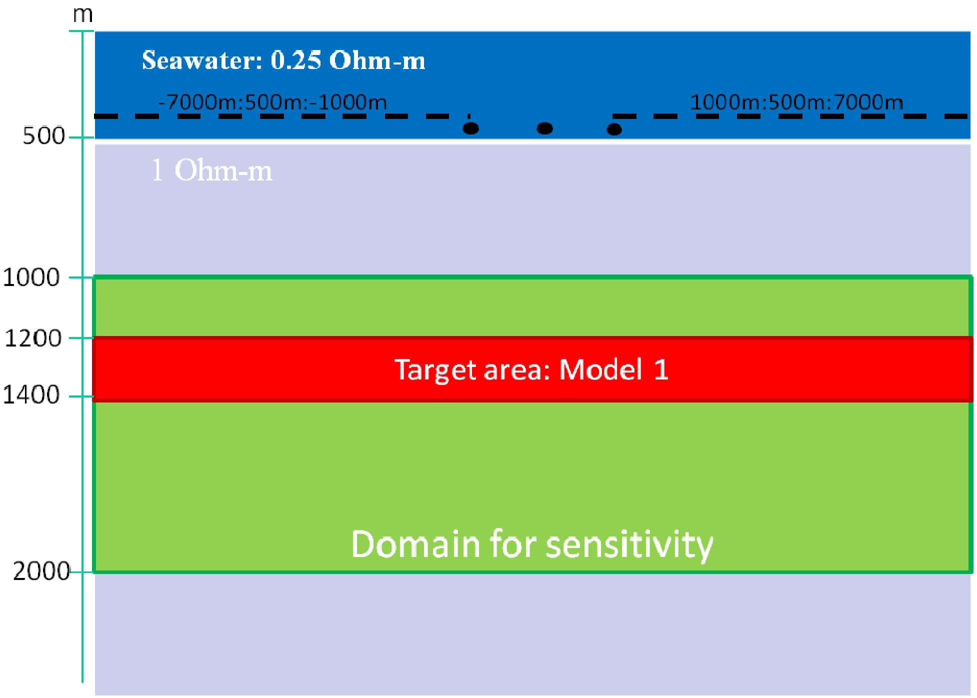

Figure 6.1. A sketch of a simple basic survey design consisting of three receivers and an electric dipole transmitter moving above this receiver in the x direction along a 14 km line with 500 m distance between transmitter points at an elevation of 50 m above the sea floor.

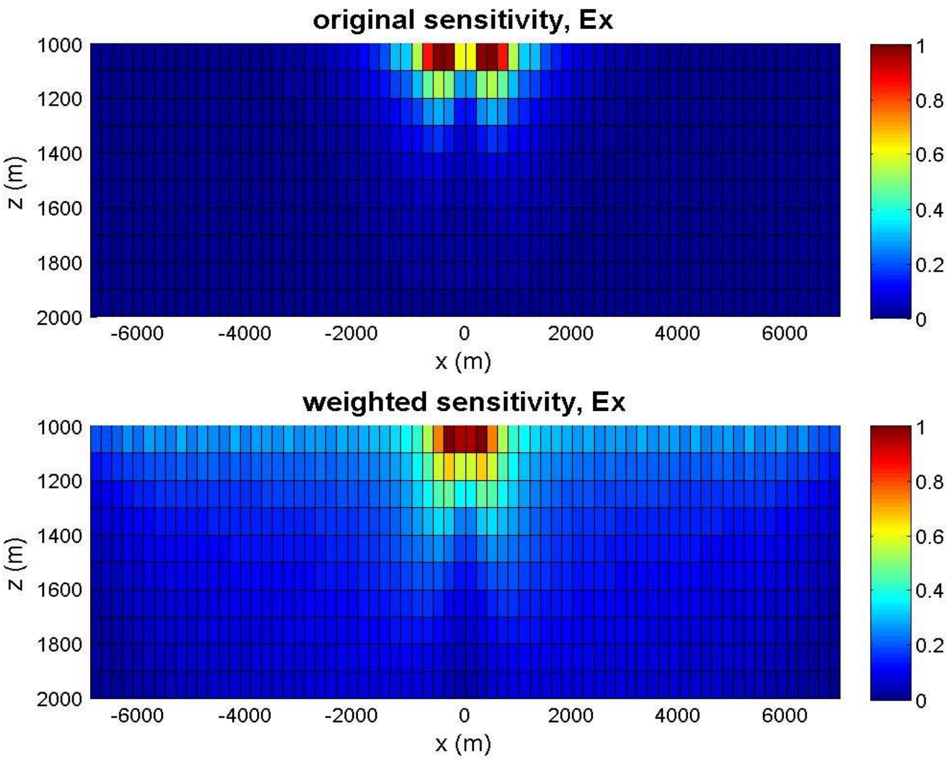

Figure 6.2. Original and weighted integrated sensitivity distributions for the basic survey consisting of one receiver, which measures the E_x component of the electric field. Both sensitivities are normalized by the corresponding maximum value. The sensitivities are computed for the E_x component, at a frequency of 0.1 Hz.

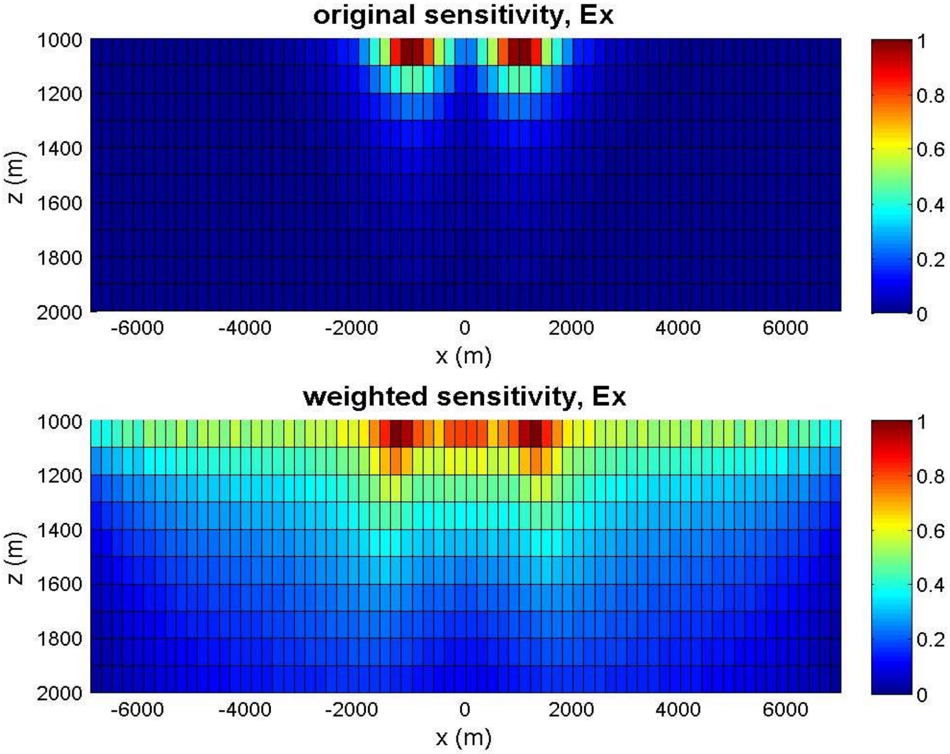

original sensitivity, Ex

weighted sensitivity, Ex

Figure 6.3. Original and weighted integrated sensitivity distributions for the basic survey consisting of three receivers, which measure the E_x component of the electric field. Both sensitivities are normalized by the corresponding maximum value. The sensitivities are computed for the E_x component, at a frequency of 0.1 Hz.

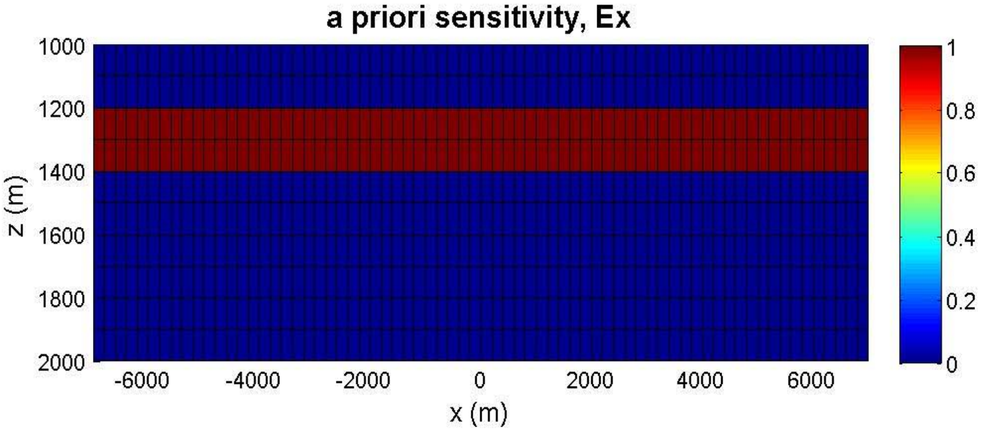

Figure 6.4. Model 1. A priori sensitivity distribution normalized by the maximum of the a priori sensitivity. The sensitivity is computed for the E_x component at a frequency of 0.1 Hz.

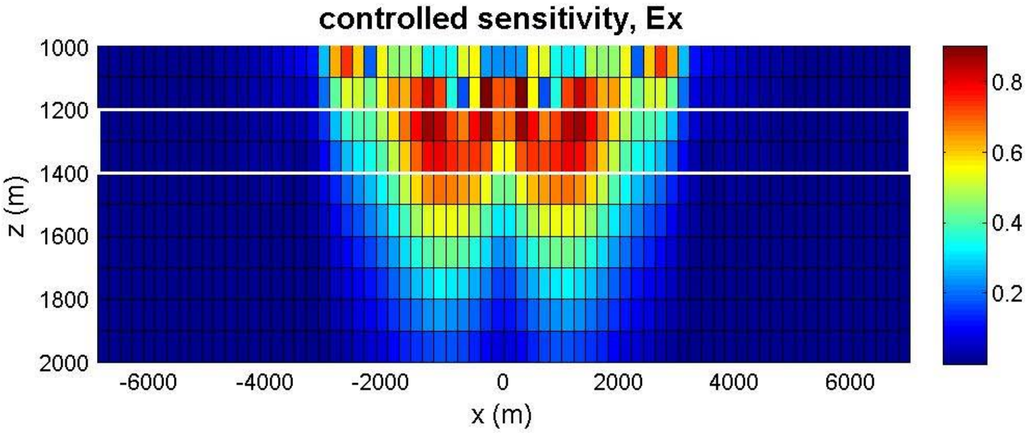

Figure 6.5. Model 1. Controlled sensitivity distribution normalized by the maximum of the a priori sensitivity. The sensitivity is computed for one receiver only, the E_x component at a frequency of 0.1 Hz.

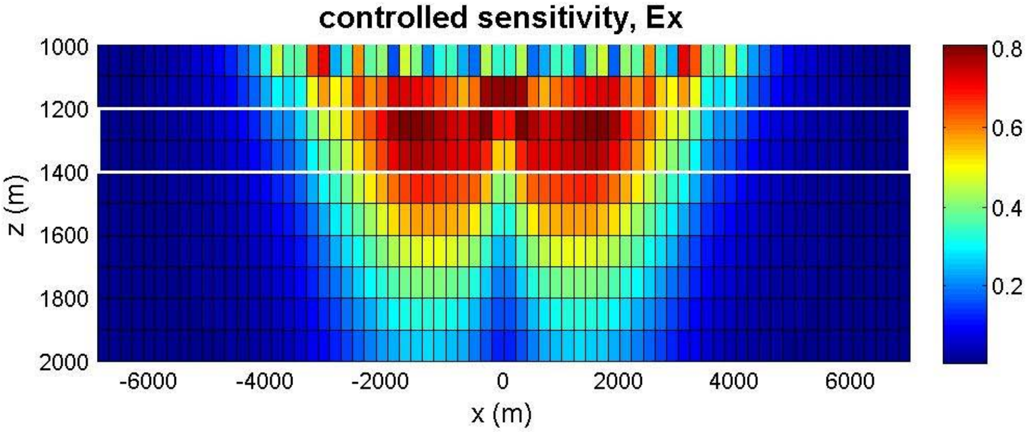

Figure 6.6. Model 1. Controlled sensitivity distribution normalized by the maximum of the a priori sensitivity. The sensitivity is computed for one receiver only, the E_x component at a frequency of 0.01 Hz.

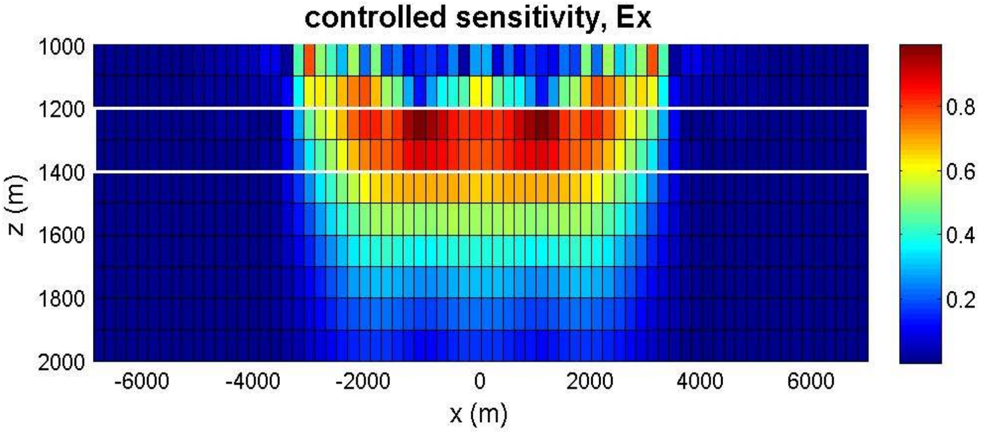

Figure 6.7. Model 1. Controlled sensitivity distribution normalized by the maximum of the a priori sensitivity. The sensitivity is computed for three receivers, the E_x component at a frequency of 0.1 Hz.

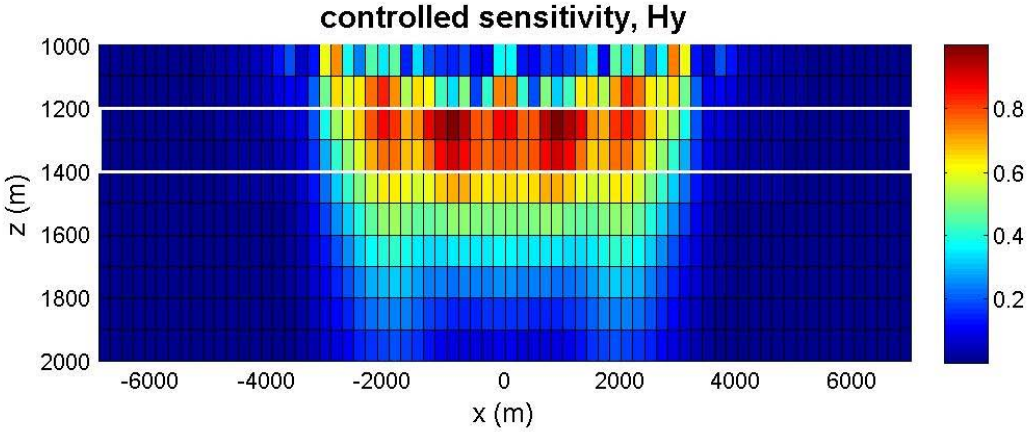

Figure 6.8. Model 1. Controlled sensitivity distribution normalized by the maximum of the a priori sensitivity. The sensitivity is computed for three receivers, the H_y component at a frequency of 0.1 Hz.

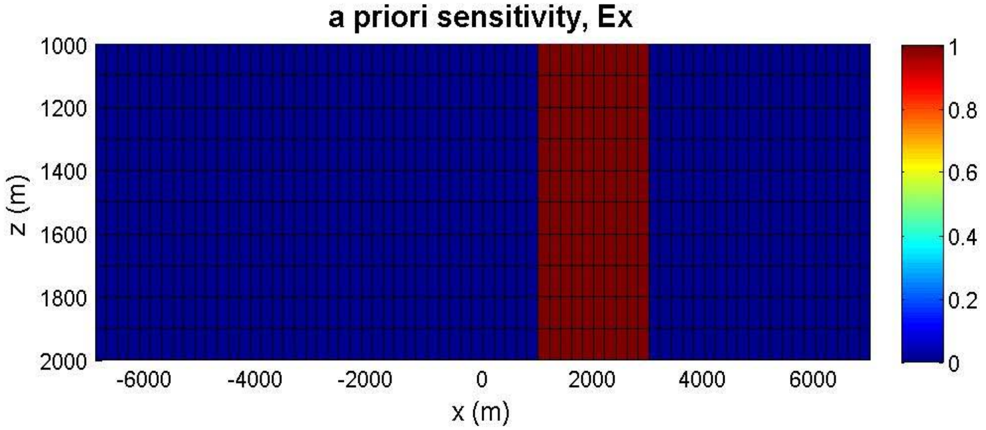

Figure 6.9. Model 2. A priori sensitivity distribution normalized by the maximum of the a priori sensitivity. The sensitivity is computed for the E_x component at a frequency of 0.1 Hz.

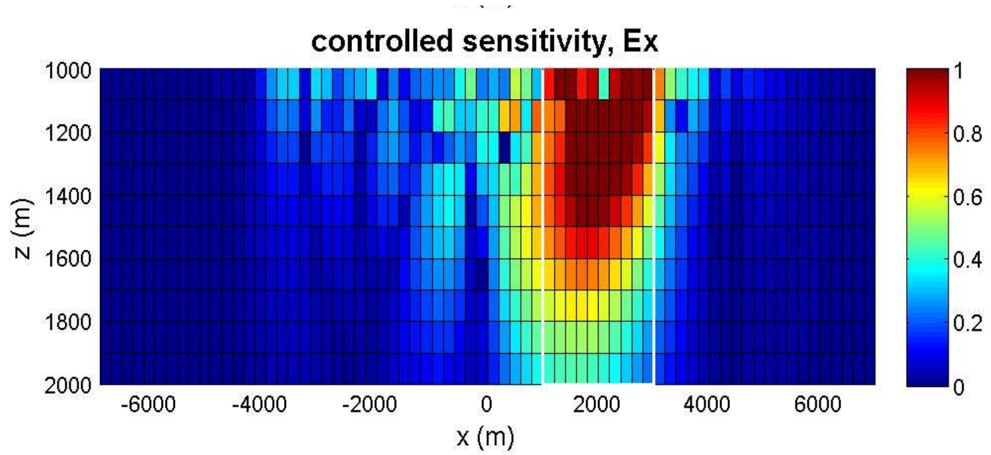

Figure 6.10. Model 2. Controlled sensitivity distribution normalized by the maximum of the a priori sensitivity. The sensitivity is computed for one receiver, the E_x component at a frequency of 0.1 Hz.

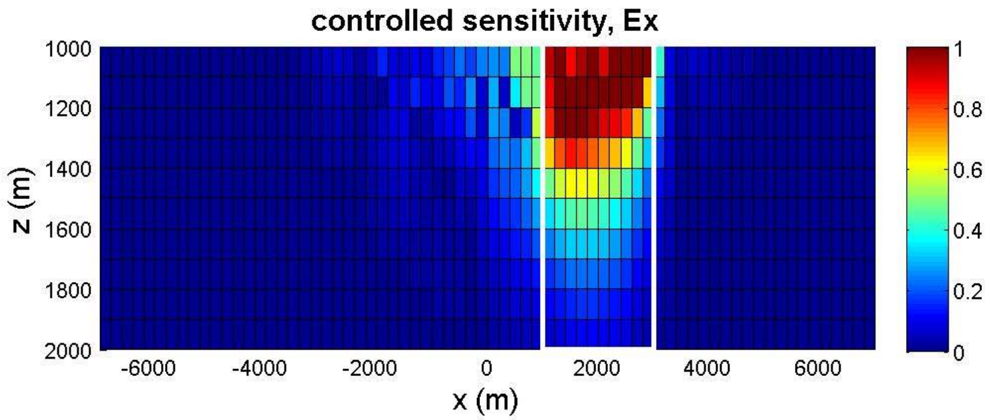

Figure 6.11. Model 2. Controlled sensitivity distribution normalized by the maximum of the a priori sensitivity. The sensitivity is computed for three receivers, the E_x component at a frequency of 0.1 Hz.

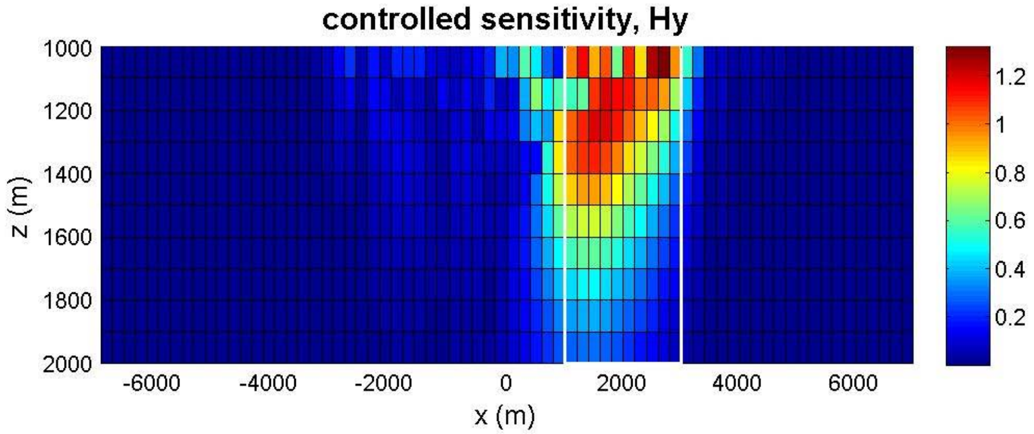

Figure 6.12. Model 2. Controlled sensitivity distribution normalized by the maximum of the a priori sensitivity. The sensitivity is computed for three receivers, the H_y component at a frequency of 0.1 Hz.

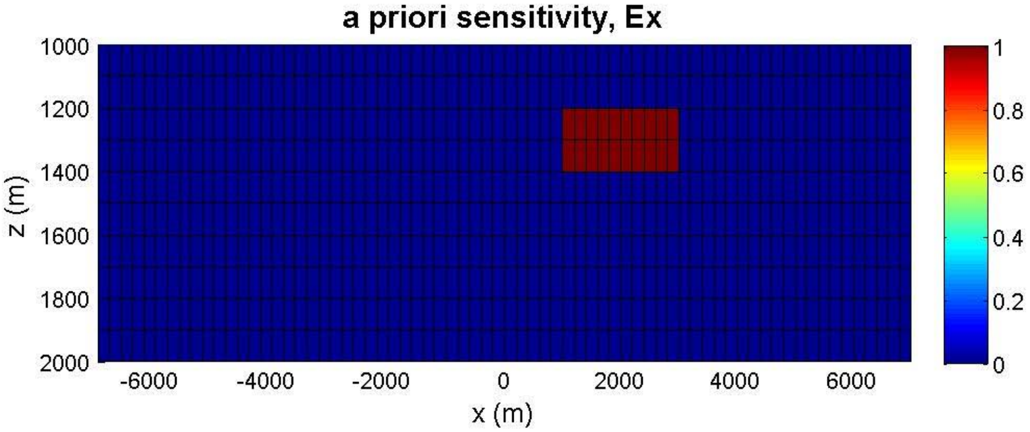

Figure 6.13. Model 3. A priori sensitivity distribution normalized by the maximum of the a priori sensitivity. The sensitivity is computed for the E_x component at a frequency of 0.1 Hz.

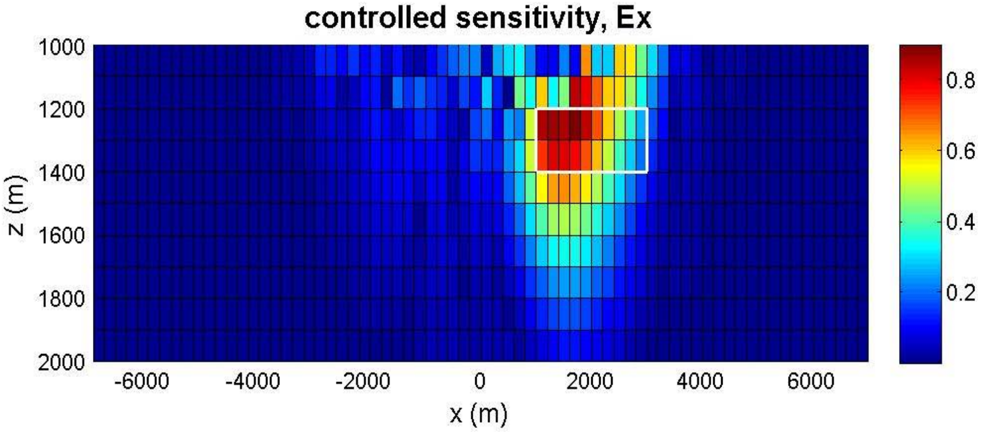

Figure 6.14. Model 3. Controlled sensitivity distribution normalized by the maximum of the a priori sensitivity. The sensitivity is computed for three receivers, the E_x component at a frequency of 0.1 Hz.

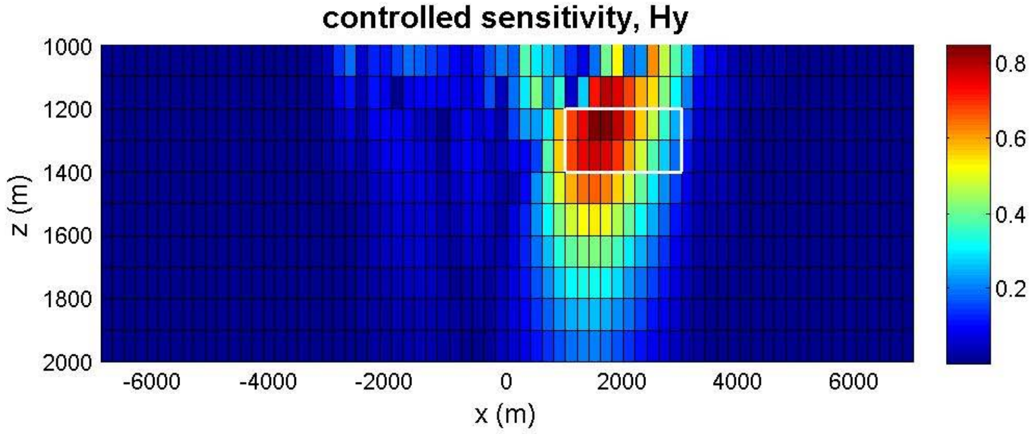

Figure 6.15. Model 3. Controlled sensitivity distribution normalized by the maximum of the a priori sensitivity. The sensitivity is computed for three receivers, the H_y component at a frequency of 0.1 Hz.

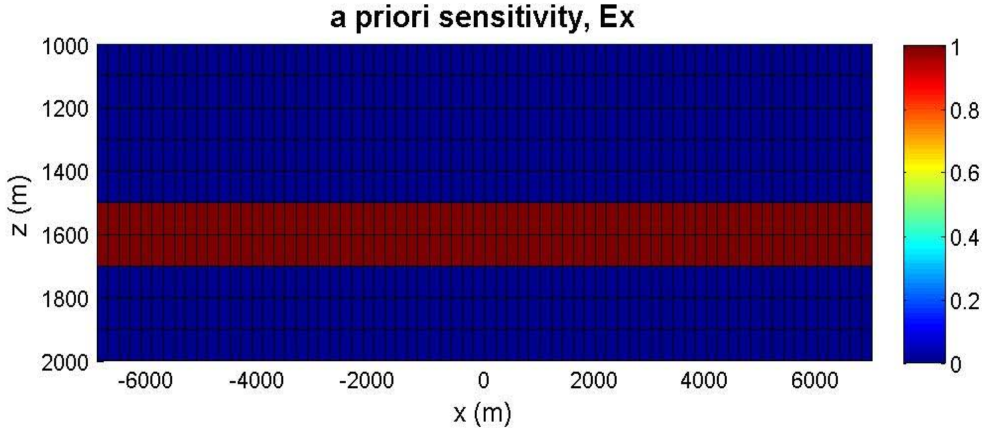

Figure 6.16. Model 2. A priori sensitivity distribution normalized by the maximum of the a priori sensitivity. The sensitivity is computed for the E_x component at a frequency of 0.1 Hz.

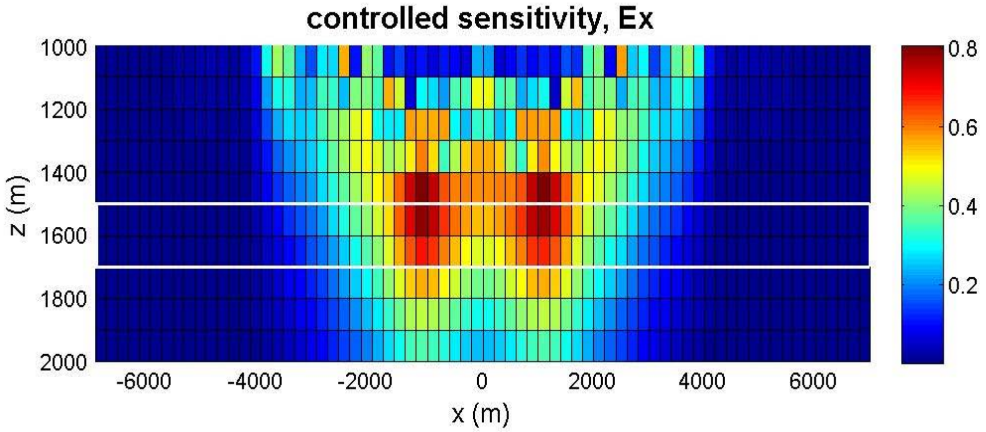

Figure 6.17. Model 4. Controlled sensitivity distribution normalized by the maximum of the a priori sensitivity. The sensitivity is computed for three receivers, the E_x component at a frequency of 0.1 Hz.

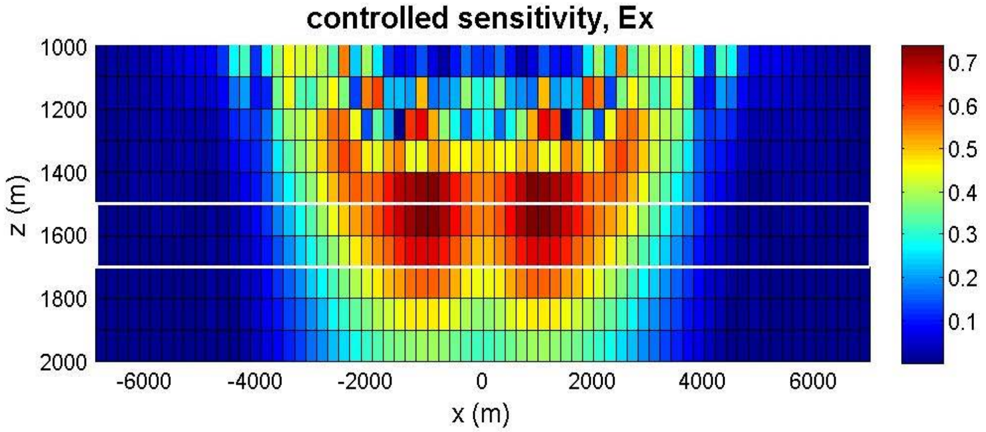

Figure 6.18. Model 4. Controlled sensitivity distribution normalized by the maximum of the a priori sensitivity. The sensitivity is computed for three receivers, the E_x component at a frequency of 0.01 Hz.

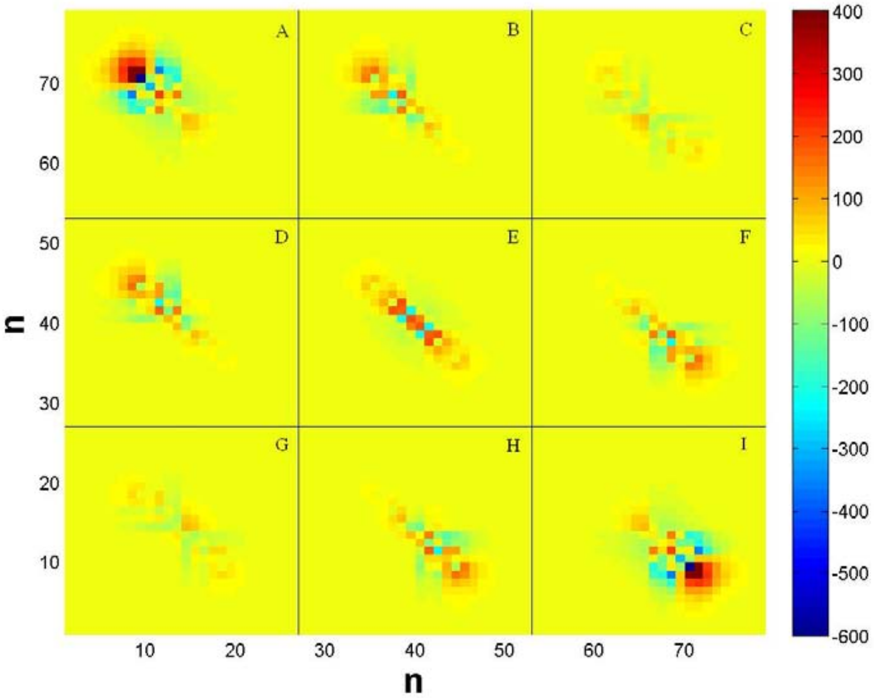

Figure 6.19. Model 1. A map of matrix Q computed for three receivers and the electric field component, E_x, at a frequency of 0.1 Hz.

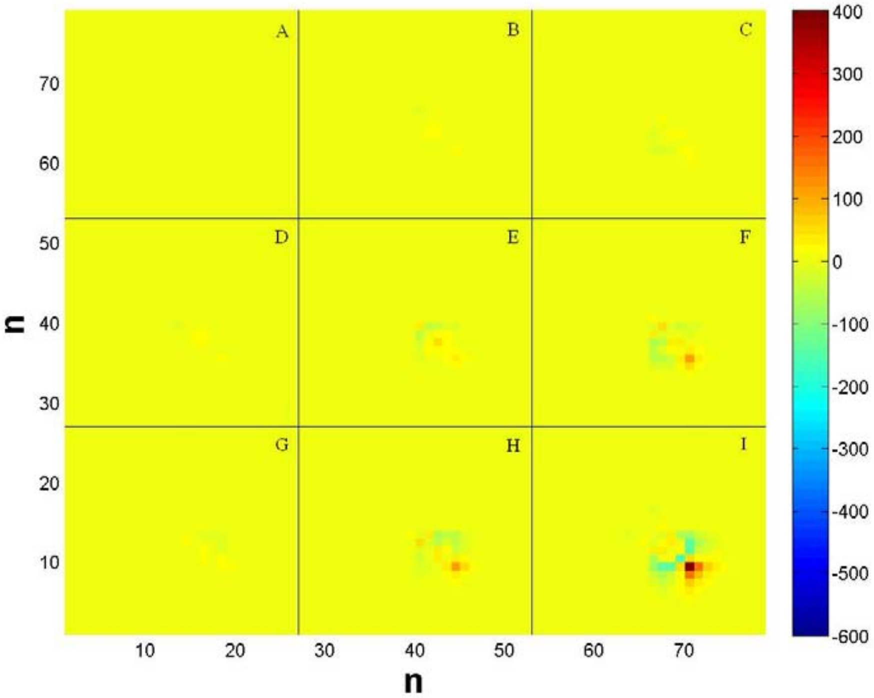

Figure 6.20. Model 2. A map of matrix Q computed for three receivers and the electric field component, E_x, at a frequency of 0.1 Hz.

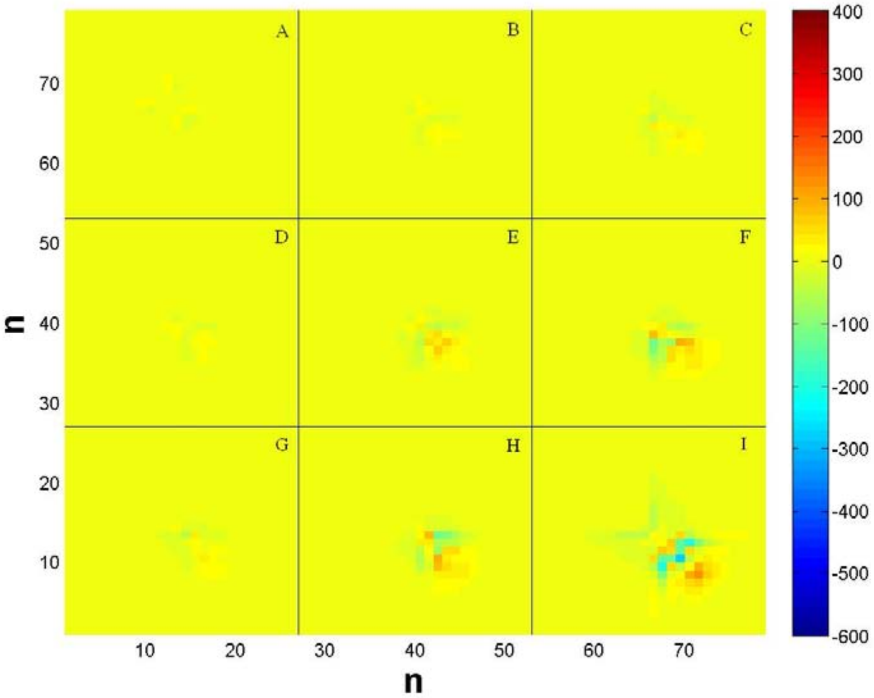

Figure 6.21. Model 3. A map of matrix Q computed for three receivers and the electric field component, E_x, at a frequency of 0.1 Hz.

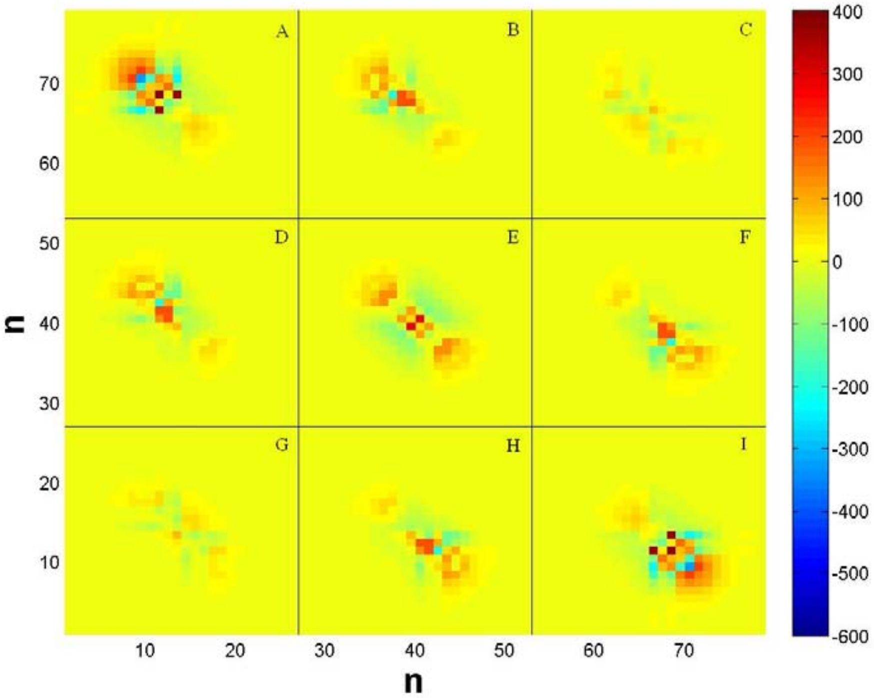

Figure 6.22. Model 4. A map of matrix Q computed for three receivers and the electric field component, E_x, at a frequency of 0.1 Hz.

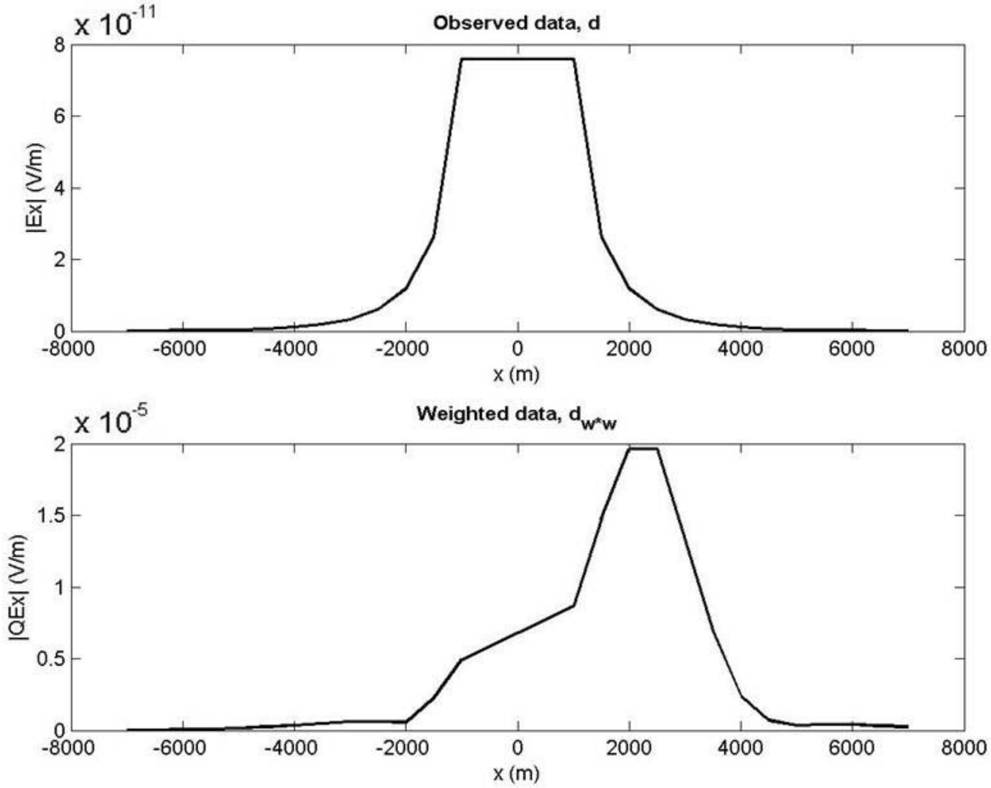

Figure 6.23. Model 2. Application of the data kernel matrix **Q** to the observed data **d** (top panel) based on the basic MCSEM survey design with three receivers. The data are computed for the E_x component at a frequency of 0.1 Hz. The weighted data (bottom panel) present the result of application of matrix **Q** to original data **d**.

CHAPTER 7

CONCLUSIONS

In this thesis, I discuss the methods of the original and weighted integrated sensitivity calculations. Those methods make it possible to evaluate a cumulative response of the observed EM data to the conductivity perturbations for a survey with a multiple transmitter/receiver observation system.

From numerical experiments for 1D and 2D original and weighted integrated sensitivities based on a simple basic MCSEM survey, I have confirmed that the obtained EM data are sensitive in the vicinity of the receiver location only and the sensitivity decreases rapidly with depth. Moreover, I demonstrate that the application of the data weighting to the data can increase the sensitivity significantly even in the far zone from the receiver location.

Based on the integrated sensitivity method, I have formulated a concept of controlled sensitivity, which enables the sensitivity of the MCSEM survey to be focused on a specific area of the sea bottom formations, where a potential target may be located. This approach is based on the optimization of the integrated sensitivity of the MCSEM survey. I have also considered a numerical method for determining the data weighting kernel matrix, which focuses the integrated sensitivity within the target area, using a linear inversion algorithm, which is based on the regularized conjugate-gradient (RCG) method.

I have demonstrated this concept with numerical studies of the 1D and 2D controlled sensitivities of the MCSEM survey. In both cases, the method successfully controls the integrated sensitivity distributions for both the E_x component of the electric field and the H_y component of the magnetic field, increasing the sensitivities within different types of the a priori selected target areas.

In these numerical studies, I have examined the effects of the survey parameters on the controlled sensitivity results. First, I have found that the frequency of a transmitted EM signal affects the controlled sensitivity result, agreeing with the skin depth effect of the EM field. When I compute the controlled sensitivity at a higher frequency, the maximum of the sensitivity increases more in the target area. I have also found that the application of controlled sensitivity method to the multifrequency data provides more focused sensitivity than for singular frequency. Second, I have also examined the controlled sensitivity for the survey data with a different number of receivers. We can observe that the data with a larger number of receivers show a better result for controlled sensitivity plot than those with only one receiver, being more focused within the target area.

In the 1D controlled sensitivity study, I have found that the data weighting kernel matrix Q has an oscillating “radiating” pattern, which indicates that the application of this matrix to the observed data may result in the predicted type of interference of the fields produced by the transmitters in different locations. This pattern has also shown in the 2D controlled sensitivity, when we divide the matrix into small sections depending on the survey information. We could see that the matrix Q controls the data, steering the data toward the target area. Thus, physically, the developed method can be described as a controlled interference of the EM fields, generated by a set of transmitters and receivers. In this sense the developed method uses physical principles similar to the synthetic aperture radar method. The main difference is that the controlled sensitivity approach is based on a rigorous optimization technique.

This method allows us to find the optimal parameters of the data weighting in order to increase the resolution of the MCSEM data within an a priori selected target area, such as the prospective location of HC reservoirs.

REFERENCES

Carazzone, J. J., O. M. Burtz, K.E. Green, and D. A. Pavlov, 2005, Three dimensional imaging of marine CSEM data: 75th Annual International Meeting, SEG, Expanded Abstract, 575-578.

Constable, S., and L. J. Srnka, 2007, An introduction to marine controlled-source electromagnetic methods for hydrocarbon exploration, Geophysics, **72**, WA3-WA12.

Cox, C. S., 1981, On the electrical conductivity of the oceanic lithosphere, Physics of the Earth and Planetary Interiors, **25**, 196–201.

Dubrovskiy, V. G., and N. V. Kondratieva, 1976, Basic results of the magnetotelluric soundings in the Turkmen sector of the Caspian Sea: Izvestia AN SSSR, Physics of the Earth, **3,** 67-76.

Edwards, N, 2005, Marine controlled source electromagnetics: principles, methodologies, future commercial applications, Geophysics, **26**, 675-700.

Edward, R. N., Nobes, D. C. and Gomez-Trevino, E. 1984, Offshore electrical exploration of sedimentary basins: the effects of anisotropy in horizontally isotropic, layered media, Geophysics, **49**, 566-576.

Eidesmo, T., S. Ellingsrud, L. M. MacGregor, S. Constable, M. C. Sinha, S. Johansen, F. N. Kong, and H. Westerdahl, 2002, Sea Bed Logging (SBL), a new method for remote and direct identification of hydrocarbon filled layers in deepwater areas: First Break, **20**, 144-152.

Fan, Y., R. Snieder, E. Slob, J. Hunziker, J. Singer, J. Sheiman, and M. Rosenquist, 2010, Synthetic aperture controlled source electromagnetics, Geophysical Research Letters, **37**, L13305, doi: 10.1029/2010GL043981.

Gribenko, A., and M. S. Zhdanov, 2007, Rigorous three-dimensional inversion of marine CSEM data based on the integral equation method, Geophysics, **72**, WA73-WA84

Hohmann, G. W., 1975, Three-dimensional induced polarization and electromagnetic modeling, Geophysics, **40**, 309-324.

Jupp, D. L. B. and Vozoff, K., 1976, Two-dimensional magnetotelluric inversion, Geophys. J. R. astr. Soc., **50**, 333-352.

Kaputerko, A., and M. S. Zhdanov, 2010, Analysis of integrated sensitivity of CSEM data in offshore hydrocarbon exploration, Proceedings of Annual Meeting of the Consortium for Electromagnetic Modeling and Inversion, 127-162.

MacGregor L. M., and M. Sinha, 2000, Use of marine controlled-source electromagnetic sounding for sub-basalt exploration, Geophysical Prospecting, **48**, 1091-1106.

McGillivray, P. R., D. W. Oldenburg, R. G. Ellis, and T. M. Habashy, 1994, Calculation of sensitivities for the frequency-domain electromagnetic problem, Geophysical Journal International, **116**, 1-4.

McGillivray, P. R., and D. W. Oldenburg, 1990, Methods for calculating Frechet derivatives and sensitivities for the nonlinear inverse problem: a comparative study, Geophysical Prospecting, **38**, 499-524.

Morten, J. P., A. K. Bjørke, and T. Støren, 2009, CSEM data uncertainty analysis for 3D inversion: 79th Annual international meeting, SEG, Expanded Abstracts, **28**, 724.

Novysh, V. V., and G. A. Fonarev, 1966, The results of the electromagnetic study in the Arctic Ocean, Geomagnetism and Aeronomy, **6**, 406-409.

Raiche, A. P., 1974, An integral equation approach to three-dimensional modeling, Geophysical Journal of the Royal Astronomical Society, **36**, 363-376.

Rodi, W. L., 1976, A technique for improving the accuracy of finite element solutions for MT data, Geophys. J. R. astr. Soc., **44**, 483-506.

Spiess, F. N., K. C. Macdonald, T. Atwater, R. Ballard, A. Carranza, D. Cordoba, C. Cox, V. M. Diaz Garcia, J. Francheteau, J. Guerrero, J. Hawkings, R. Haymon, R. Hessler, T. Juteau, M. Kastner, R. Larson, B. Luyendyk, J. D. Macdougall, S. Miller, W. Normark, J. Orcutt, and C. Rangin, 1980, East Pacific Rise: Hot spring sand geophysical experiments, Science, **207**, 1421–1433.

Trofimov, I. L., and G. A. Fonarev, 1972, Some results of the magnetotelluric profilinf in the Arctic ocean: Izvestia AN SSSR, Physics of the Earth, (2), 81-92.

Weidelt, P., 1975a, Electromagnetic induction in three-dimensional structures, Jounal of Geophysics, **41** (1), 85-109.

Young, P. D., and C. S. Cox, 1981, Electromagnetic active source sounding near the East Pacific Rise, Geophysical Research Letters, **8**, 1043–1046.

Zhdanov, M. S., 2002, Geophysical inverse theory and regularization problems, Elsevier.

Zhdanov, M. S., 2009, Geophysical electromagnetic theory and methods, Elsevier.

Zhdanov, M. S., 2010, Electromagnetic geophysics: Notes from the past and the road ahead, Geophysics, **75**, 49-66.